

Fabrication and Characterization of Graphene-Based Heterostructure using
Molybdenum as Alternative Electrodes



A Thesis Submitted in Partial Fulfillment of the Requirements

for the Degree of Master of Science in Physics

Department of Physics

FACULTY OF SCIENCE

Chulalongkorn University

Academic Year 2020

Copyright of Chulalongkorn University

การประดิษฐ์และการศึกษาสมบัติของสารสังเคราะห์ที่มีโครงสร้างหลายชั้นจากกราฟีน โดยใช้
โพลีบดีนัมเป็นขั้วไฟฟ้าทางเลือก



วิทยานิพนธ์นี้เป็นส่วนหนึ่งของการศึกษาตามหลักสูตรปริญญาวิทยาศาสตรมหาบัณฑิต
สาขาวิชาฟิสิกส์ ภาควิชาฟิสิกส์
คณะวิทยาศาสตร์ จุฬาลงกรณ์มหาวิทยาลัย
ปีการศึกษา 2563
ลิขสิทธิ์ของจุฬาลงกรณ์มหาวิทยาลัย

อิลเลียส คลานูร์กี : การประดิษฐ์และการศึกษาสมบัติของสารสังเคราะห์ที่มีโครงสร้างหลายชั้น
จากกราฟีน โดยใช้โมลิบดีนัมเป็นขั้วไฟฟ้าทางเลือก. (Fabrication and Characterization of
Graphene-Based Heterostructure using Molybdenum as Alternative Electrodes) อ.ที่
ปรึกษาหลัก : ผศ. ดร.ธิตี เตชธนพัฒน์

อันตรกิริยาระหว่างชั้นของกราฟีนสามารถนำไปใช้ปรับแต่งสมบัติการถ่ายโอนประจุไฟฟ้าผ่าน
ตัวนำ สำหรับการนำไปประยุกต์ใช้ในงานด้านนาโนอิเล็กทรอนิกส์ กราฟีนมักจะถูกนำมาหุ้มด้วยแผ่นโบรอน
ไนไตรด์ที่มีโครงสร้างผลึกแบบหกเหลี่ยมเพื่อเพิ่มประสิทธิภาพให้กับอุปกรณ์อิเล็กทรอนิกส์ และมักจะมี
ขั้วไฟฟ้าที่สร้างจากทองคำบนฟิล์มบางของโครเมียม (Cr/Au) ในงานวิจัยครั้งนี้ โมลิบดีนัม (Mo) ได้ถูก
นำมาใช้เป็นขั้วไฟฟ้าทางเลือกเพื่อลดความซับซ้อนของกระบวนการผลิต เราได้พัฒนากระบวนการ
ประดิษฐ์ทรานซิสเตอร์สนามไฟฟ้า (Field-effect transistor, FET) จากแผ่นกราฟีนคู่ที่ถูกรบิด (Twisted
bilayer graphene, tBLG) ขั้วไฟฟ้า Mo ได้ถูกนำมาเชื่อมกับขอบของกราฟีนโดยใช้เทคนิคสปัตเตอริง
(sputtering) เกิดเป็นหน้าสัมผัสทางไฟฟ้าแบบหนึ่งมิติตรงของกราฟีน การตรวจวัดการถ่ายโอน
อิเล็กตรอนได้ถูกนำมาใช้กับ FET ที่ถูกสร้างขึ้นเพื่อตรวจสอบคุณภาพของหน้าสัมผัส จากการทดลองพบว่า
หน้าสัมผัสระหว่าง Mo กับกราฟีนเป็นหน้าสัมผัสแบบโอห์มมิก (Ohmic contact) โดยสภาพต้านทานไฟฟ้า
หน้าสัมผัสมีค่าสูงสุดที่ประมาณ $1,300 \Omega \cdot \mu\text{m}$ เมื่อกราฟีนอยู่ในสภาพที่ไม่มีประจุพาหะ และค่อย ๆ ลดลง
ถึง $975 \Omega \cdot \mu\text{m}$ เมื่อประจุพาหะในกราฟีนมีค่าเพิ่มขึ้นจนมีความหนาแน่นประมาณ $4 \times 10^{12} \text{ cm}^{-2}$ อย่างไรก็ตาม
ตามสภาพต้านทานหน้าสัมผัสที่วัดได้มีค่าเพิ่มขึ้นตามกาลเวลา ซึ่งคาดว่าน่าจะเป็นผลมาจากการออกซิไดซ์
ของ Mo จากการศึกษพบว่าหลังจากเวลาผ่านไปสามเดือน หน้าสัมผัส Mo ยังคงมีพฤติกรรมแบบโอห์มมิก
แม้ว่าจะมีสภาพต้านทานที่เพิ่มขึ้น ซึ่งสามารถใช้ตรวจสอบการถ่ายโอนประจุใน tBLG ได้ จากการตรวจสอบ
พบว่า tBLG มีสภาพคล่องตัว (mobility) ของอิเล็กตรอนและโฮลที่อุณหภูมิห้องสูงถึง 27,000 และ 21,000
 $\text{cm}^2/\text{V}\cdot\text{s}$ ซึ่งบ่งชี้ให้เห็นว่าขั้วไฟฟ้า Mo ไม่ได้ลดคุณภาพของการถ่ายโอนประจุในกราฟีน

สาขาวิชา ฟิสิกส์

ปีการศึกษา 2563

ลายมือชื่อนิสิต

ลายมือชื่อ อ.ที่ปรึกษาหลัก

6172109423 : MAJOR PHYSICS

KEYWORD: Graphene, Van der Waals heterostructures, Molybdenum electrodes, One-dimensional edge contacts

Illias Klanurak : Fabrication and Characterization of Graphene-Based Heterostructure using Molybdenum as Alternative Electrodes. Advisor: Asst. Prof. Dr. Thiti Taychatanapat

Interlayer coupling in graphene heterostructures can be used to modify their charge transport properties for the use in nanoelectronics applications. To achieve high-performance devices, graphene is typically encapsulated by two thin sheets of hexagonal boron nitride (hBN) and contacted using Cr/Au as electrodes. In this research, Mo was selected as alternative stand-alone electrodes to simplify the fabrication process. We have developed a recipe for the fabrication of field-effect transistor (FET) using twisted bilayer graphene (tBLG) as a transport channel. Mo was employed to make one-dimensional (1D) contacts to the edges of graphene by sputtering. Electronic transport measurement was then performed on the FET devices to investigate the quality of Mo contacts. We achieved ohmic contacts between Mo and graphene. The contact resistivity between Mo and graphene reached a maximum value of around $1,300 \Omega \cdot \mu\text{m}$ at charge neutrality point and decreased to $975 \Omega \cdot \mu\text{m}$ at a carrier density of $\sim 4 \times 10^{12} \text{ cm}^{-2}$. However, we have observed that the contact resistivity increases over time likely due to the oxidization of Mo. Despite the increase in contact resistivity, the Mo contacts still exhibit ohmic behavior after 3 months and it can be used to investigate transport phenomena in graphene. In this study, the room-temperature electron and hole mobilities of tBLG reached values as high as 27,000 and 21,000 $\text{cm}^2/\text{V}\cdot\text{s}$ indicating that Mo electrodes do not hinder the transport characteristics of graphene.

Field of Study: Physics

Student's Signature

Academic Year: 2020

Advisor's Signature

ACKNOWLEDGEMENTS

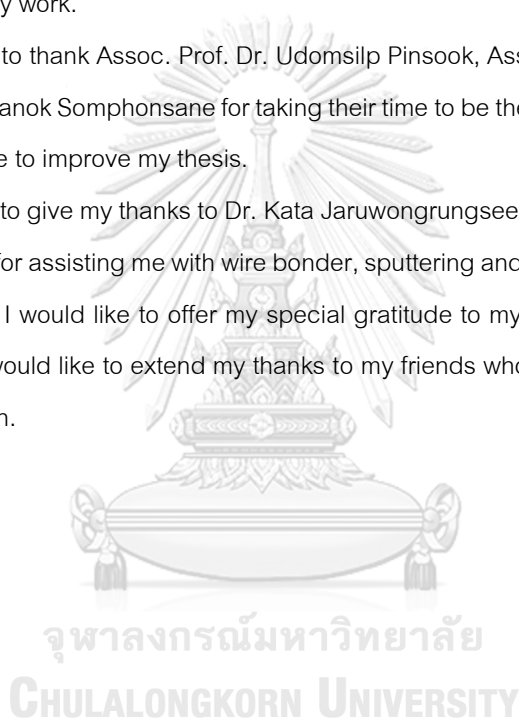
I would first like to express my deepest gratitude to my advisor, Asst. Prof. Dr. Thiti Taychatanapat, for investing his time to support me in this work. His invaluable advice and profound guidance carried me through my academic years. Without his dedication, this thesis would not have been complete.

I am deeply grateful to Asst. Prof. Dr. Sojiphong Chatraphorn to allow me to use the lab, advanced scientific instruments and other equipment for doing my research. His insightful suggestions were very helpful to my work.

I would like to thank Assoc. Prof. Dr. Udomsilp Pinsook, Assoc. Prof. Dr. Satreerat Hodak and Assoc. Prof. Dr. Ratchanok Somphonsane for taking their time to be the members of my thesis committee and their useful advice to improve my thesis.

I would like to give my thanks to Dr. Kata Jaruwongrunsee, Dr. Boonyaluk Namnuan and Mr. Pornsak Panchawirat for assisting me with wire bonder, sputtering and e-beam lithography, respectively.

In addition, I would like to offer my special gratitude to my parents who always support and believe in me. I also would like to extend my thanks to my friends who are always there to rest my mind outside of my research.



Illias Klanurak

TABLE OF CONTENTS

	Page
.....	iii
ABSTRACT (THAI).....	iii
.....	iv
ABSTRACT (ENGLISH)	iv
ACKNOWLEDGEMENTS.....	v
TABLE OF CONTENTS.....	vi
1 Introduction.....	1
1.1 Overview	1
1.2 Research objectives	3
1.3 Thesis outline	3
2 Theoretical Overview.....	4
2.1 Graphene and its electronic properties	4
2.2 Raman spectroscopy	11
2.3 Charge transportation in graphene-FET devices.....	15
3 Device Fabrication	18
3.1 Graphene and hBN exfoliation	18
3.2 2D material flakes identification	19
3.3 BNGBN assembly.....	22
3.3.1 Stamp preparation.....	22
3.3.2 Tear-and-stack technique	23
3.3.3 Raman spectroscopy	27

3.4 Electron-beam lithography	29
3.4.1 Resist spinning	29
3.4.2 Electron-beam exposure and resist development.....	30
3.5 Plasma Etching	32
3.6 Molybdenum deposition	34
3.6.1 EBL for writing contacts patterns	34
3.6.1 Mo sputtering	36
3.6.1 Lift-off process.....	37
3.7 Wire bonding	39
4 Transport Measurements	40
4.1 Experimental setup.....	40
4.1.1 DC measurement	41
4.1.1 AC measurement.....	42
4.2 Mo Contact Characterization.....	43
4.3 Charge transportation in tBLG	46
5 Conclusions	49
REFERENCES.....	51
VITA	56

Chapter 1

Introduction

1.1 Overview

Silicon-based semiconductor technology has brought unprecedented change to our modern civilization. The main reason for this advancement is the miniaturization of semiconductor devices which is a process in which components in the electronic devices are scaled down to smaller sizes. The miniaturization enables more electronic components to be packed into a single chip resulting in more computing power with less power consumption. As the miniaturization is progressing toward the theoretical limits, quantum effects become obstacles for electron transport in semiconductor devices [1]. These limitations inspire scientists to invent new kinds of devices that work in different ways from the traditional ones, e.g., using the quantum effect as a principle for device operation. To realize the next-generation devices, new materials that possess unique electronic properties are required to replace silicon in semiconductor technology.

Two-dimensional (2D) materials have gained enormous interest in the past decade due to their remarkable electrical and mechanical properties [2]. Graphene, a 2D layer of carbon atoms arranged in a honeycomb lattice, is the first 2D material that was extensively studied. After its first discovery in 2004 [3], researchers have observed many exotic phenomena such as half-integer quantum Hall effect [4], Klein tunneling [5], tunable bandgap [6], etc. The intrinsically high-mobility and high-mechanical strength of graphene makes graphene a suitable candidate for many applications such as sensors, memory devices, wearable electronics, etc. [7]. In 2018, Yuan Cao et al. published a report for the observation of superconducting state in twisted bilayer graphene (tBLG) [8], marking a new milestone for 2D materials research. This observation showed an unusual behavior that cannot be explained by a free or weakly interacting electron model indicating that it was a result of a strongly interacting electron system. tBLG sparks an interest to study a relation between a twist angle between two layers of 2D materials and their electronic

properties. Nevertheless, to observe these exotic phenomena, a high-quality device, i.e., a device with low defect and high mobility, is a crucial requirement.

The main 2D material that was focused on in this thesis is graphene. In the early stage of graphene research, high-quality graphene devices were obtained by mechanical exfoliation and typically deposited onto a silicon wafer with a thin oxidized layer of SiO₂ [3-6]. However, the surface of SiO₂ substrate usually contains undesirable trapped charges causing spatial inhomogeneity of charge density in graphene, the so-called electron-hole puddles, near charge neutrality point [9]. The formation of electron and hole puddles in addition to a scattering of charge carriers with charge impurities and surface roughness of SiO₂ limit charge carrier mobility in graphene resulting in a poor performance graphene device. Furthermore, the scattering of charge carriers in graphene with the impurities may disturb quantum effects making it impossible to probe intrinsic characteristics of the system. The effective way to overcome these issues is to use hexagonal boron nitride (hBN) as a substrate for graphene instead of SiO₂ [10].

To completely separate graphene layer from extrinsic impurities, two hBN sheets may be used to encapsulate graphene layer. This encapsulated structure, consisting of a vertical stack of different 2D materials, is called van der Waals heterostructure. The heterostructure imposes a new limitation for making electrical contacts between graphene and metal electrodes since graphene is embedded in the insulating layers of hBN. One way to overcome this limitation is to expose the edge of graphene by using O₂/CHF₃ plasma to etch the heterostructure. Then, metal electrodes are deposited onto the heterostructure, making one-dimensional contact with the edge of graphene [11]. In this thesis, this contact geometry is referred to as edge-contact.

One of the crucial factors to determine the quality of contact is contact resistance which is a resistance that arises from voltage drop when charge carriers are transferred between the interface of graphene and metal electrode. Even though edge-contact can enhance the transport properties of graphene, it requires specific metals to make intimate contact with graphene edge. Typically, Au is used together with Cr adhesion layer to make intimate contact with graphene due to its low contact resistance. The adhesion layer is essential for this geometry since Au does not stick very well to the edge of graphene making it unreliable to be a stand-alone electrode for graphene as demonstrated in the

supplementary material of Ref.[11]. The high work function of Au (5.1 eV) may also limit graphene versatility to integrate with other 2D materials such as MoS₂ since it may result in Schottky barrier at the Au-semiconductor interface.

In this thesis, Mo was selected as an alternative stand-alone cheaper electrode to make edge-contact with graphene. The ability of Mo to form a covalent bond with the carbon atom of graphene [12] enables the realization of the contact without an adhesion layer. The carbide formation between Mo and graphene may also enhance orbital overlap at the Mo-C interface which is an important factor for making high-quality contact [11]. A lower work function of Mo (4.5 eV) compared to Au make it easier to realize ohmic contact [13] increasing the flexibility of graphene to be integrated with other 2D materials. To characterize the quality of Mo edge-contact, field-effect transistors (FETs) using tBLG as transport channels and Mo as metal electrodes were fabricated. Electronic transport measurement was then performed on the devices to investigate the quality of Mo edge-contact and transport characteristics of tBLG.

1.2 Research objectives

- (i) To fabricate field-effect transistor (FET) based on hBN-encapsulated tBLG using Mo as edge-contact
- (ii) To characterize the quality of Mo edge-contacts
- (iii) To investigate electronic transport properties of tBLG using electronic transport measurement at room temperature

1.3 Thesis outline

In the next chapter, we will explore a theoretical overview of the research. This includes electronic properties of graphene, characterization of graphene using Raman spectroscopy, basic principles of FET and charge transportation on graphene devices. Chapter 3 explains the fabrication process starting from mechanical exfoliation of graphene and hBN flakes to the final FET device. Chapter 4 investigates the transport properties of tBLG and the quality of Mo contacts. Finally, the conclusions of the thesis will be given in chapter 5.

Chapter 2

Theoretical Overview

This chapter provides an overview of important concepts using throughout the thesis. It covers a wide range of topics starting with basic knowledge of graphene, mainly focused on its electronic properties. A brief review of twisted bilayer graphene is also present in this section. Next, we will explore Raman spectroscopy, a powerful technique used for graphene characterization. Then charge transportation in graphene devices will be explained.

2.1 Graphene and its electronic properties

Graphene is a building block of graphite, a material that is used as pencil lead. Graphite is one of the carbon allotropes, consisting of a stack of layered materials called graphene. Carbon atoms in the same layer of graphene are connected to their neighboring carbon atoms by strong covalent bonds. However, each layer of graphene is attached to other layers by weak van der Waals interactions as shown in Figure 2.1(a) making it easy to isolate the graphene layer from the bulk graphite. The first isolation of single-layer graphene was done by Novoselov *et al.* in 2004 using the mechanical exfoliation method, also known as the “scotch tape” technique [3]. The exfoliation method works by sticking a piece of bulk graphite to one end of a strip of adhesive tape. After the bulk graphite has been pulled out from the tape, some of the thin graphite flakes will adhere to the tape. The region of the tape with the graphite flakes is then brought into contact with the other end of the strip and peel off creating, even more, thinner graphite flakes at both ends. Repeating this step a few times, one obtains small flakes with some of them having a thickness of only a single layer of atoms. Finally, the adhesive tape with graphene flakes is brought into contact with a desired substrate and peel off leaving the graphene flakes on that substrate. The discovery of this simple technique marks the beginning of a new era of 2D materials research.

In the early days of 2D materials research, graphene intrigued scientists and researchers due to its unique mechanical [14] and electrical properties [3, 5, 6, 15]. Its unusual electronic properties can be derived from its lattice structure which consists of carbon atoms arranged in a honeycomb lattice as shown in Figure 2.1(b). The electron configuration of an isolated carbon atom can be written as $1s^2 2s^2 2p^2$. The four valence electrons are responsible for the formation of covalent bonds with neighboring carbon atoms. In the covalent bond formation process, one electron from 2s orbital is promoted to $2p_z$ orbital which is a dumbbell-shaped orbital that has an axis perpendicular to the graphene plane. The remaining one electron in 2s orbital along with two electrons in $2p_x$ and $2p_y$ orbitals form three hybridized sp^2 orbitals with degenerate energy levels. The sp^2 orbitals have axis lied in the graphene plane separated from each other by 120° (Figure 2.1(c)). The sp^2 orbitals of each carbon atom form σ bonds with sp^2 orbitals of the neighboring atoms resulting in a hexagon-shaped pattern of graphene. The electron in the $2p_z$ orbital also forms π bond with the $2p_z$ electron from the neighboring atom.

The honeycomb lattice can be seen as a triangular Bravais lattice with two basis, A and B. The carbon atoms in each sublattice are connected by lattice vectors

$$\mathbf{a}_1 = a_0 \mathbf{e}_x \quad \text{and} \quad \mathbf{a}_2 = \frac{a_0}{2} (\mathbf{e}_x + \sqrt{3}\mathbf{e}_y), \quad (2.1)$$

where $a_0 = \sqrt{3}a = 0.246$ nm is a lattice constant and $a = 0.142$ nm is a nearest C–C distance. The reciprocal lattice vectors corresponding to the triangular Bravais lattice are

$$\mathbf{b}_1 = \frac{2\pi}{a_0} \left(\mathbf{e}_x - \frac{\mathbf{e}_y}{\sqrt{3}} \right) \quad \text{and} \quad \mathbf{b}_2 = \frac{4\pi}{\sqrt{3}a_0} \mathbf{e}_y \quad (2.2)$$

satisfying the condition

$$\mathbf{a}_i \cdot \mathbf{b}_j = 2\pi\delta_{ij}. \quad (2.3)$$

Figure 2.1(d) shows reciprocal lattice points in momentum space centered at $\mathbf{k} = 0$, the so-called Γ point. The shaded region is the first Brillouin zone (BZ) consists of six BZ corners labeled by K and K' . Each K (or K') point at the BZ corners is equivalent to each other since it can be connected by the reciprocal lattice vectors. However, K and K' points are inequivalent and they represent different electronic states. K and K' are located at

$$\mathbf{K} = \frac{4\pi}{3a_0} \mathbf{e}_x \quad \text{and} \quad \mathbf{K}' = -\frac{4\pi}{3a_0} \mathbf{e}_x \quad (2.4)$$

in momentum space.

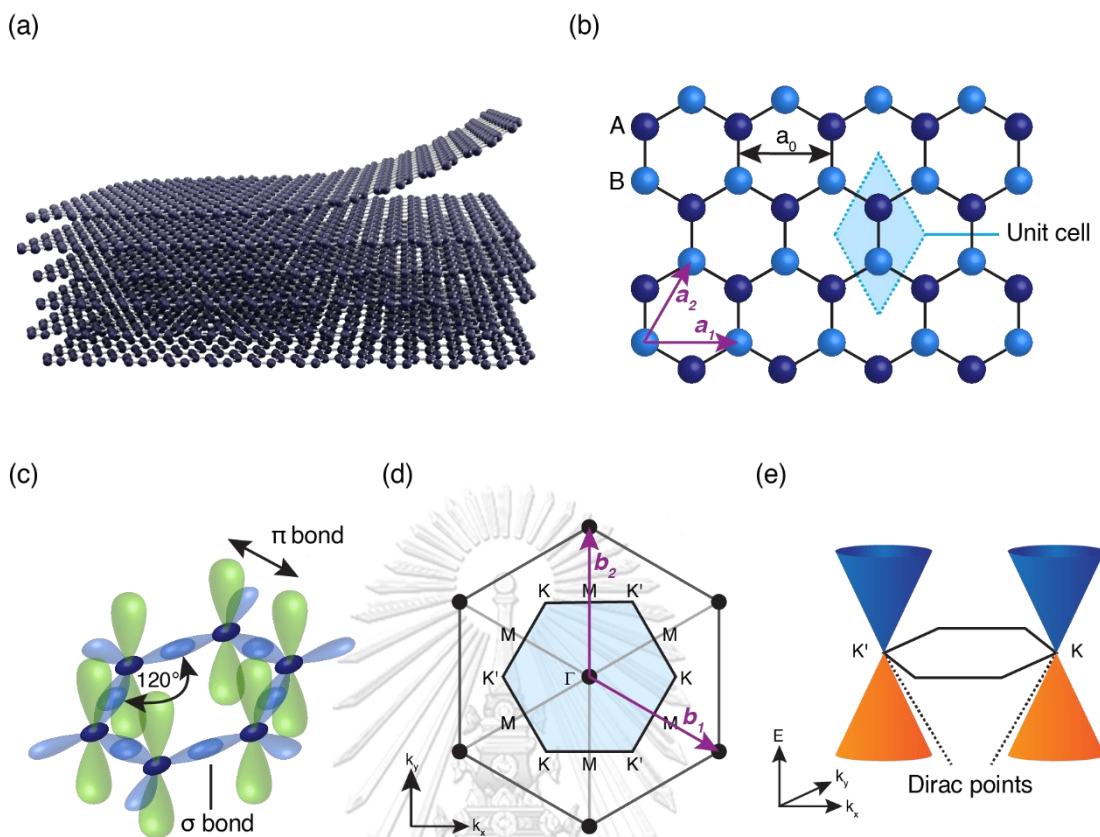


Figure 2.1(a) Graphite structure consists of a stack of graphene layers holding to the nearby layers with weak van der Waals forces. (b) Crystal structure of monolayer graphene. The shaded area indicates the unit cell of the triangular lattice with lattice constant a_0 . The dark blue and blue spheres represent carbon atoms in two different sublattices A and B respectively. (c) Illustration of hybridized orbital shape in a hexagonal ring of graphene. (d) The reciprocal lattice of monolayer graphene centered at Γ point. The black dots represent points in k -space that is equivalent to the Γ point. The shaded region is the first Brillouin zone labeled with various high symmetry points. (e) Electronic band structure of monolayer graphene at low energy. The Fermi energy of undoped graphene is located at the touching between conduction bands and valent bands called Dirac points.

The electronic band structure of graphene was first predicted by P. R. Wallace in 1947 using tight-binding approximation [16]. Since many interesting phenomena observed in graphene are results of charge transport at low energy, we will only explore the band structure in the vicinity of K and K' points which are the points that Fermi energy is lying for undoped graphene. In this case, only electrons in the $2p_z$ orbital are taken into account for the band structure calculation since electrons in the sp^2 orbitals create energy bands far away from the Fermi energy. Practically speaking, each carbon atom contributes only one electron to the band structure.

The electronic band structure of monolayer graphene (MLG) can be described by the low energy effective Hamiltonian

$$H_{\text{MLG}} = \begin{pmatrix} v_0 \boldsymbol{\sigma} \cdot \mathbf{p}_K & 0 \\ 0 & -v_0 \boldsymbol{\sigma} \cdot \mathbf{p}_{K'} \end{pmatrix} \quad (2.5)$$

where v_0 is Fermi velocity (10^6 m/s for MLG), $\boldsymbol{\sigma} = (\sigma_x, \sigma_y, \sigma_z)^T$ and σ_i are Pauli matrices, $\mathbf{p}_K = \hbar(\mathbf{k} - K)$ and $\mathbf{p}_{K'} = \hbar(\mathbf{k} - K')$ are momentum measured away from K and K' points respectively, and \hbar is reduced Plank's constant. This Hamiltonian acts on a four-spinor representation of the electronic state $\Psi = (\psi_{A,K}, \psi_{B,K}, \psi_{B,K'}, \psi_{A,K'})^T$, where the components $\psi_{A(B),K}$ and $\psi_{A(B),K'}$ are wavefunction amplitudes of an electron in A(B) sublattice near K and K' points, respectively. The diagonal terms, $v_0 \boldsymbol{\sigma} \cdot \mathbf{p}_K$ and $-v_0 \boldsymbol{\sigma} \cdot \mathbf{p}_{K'}$ are MLG Hamiltonians describing electronic states in the vicinity of K and K' points. The vanishing of off-diagonal terms indicates a decoupling between K and K' states at low energy. As a result, K and K' can be treated as good quantum numbers, typically known as "valley index".

The Hamiltonian in Equation (2.5) gives rise to a band structure of MLG at low energy ($E < 1$ eV). The band structure consists of two cone-shaped dispersions, called Dirac cones, touching each other at K and K' points as shown in Figure 2.1(e). The upper and lower Dirac cones represent conduction and valence bands forming valley shapes at K and K' points. Fermi energy of undoped pristine MLG is located at the touching points between these conduction bands and valence bands, called Dirac points, which are set to be zero. As a result, the Fermi surface of undoped MLG is just 2 points located at K and K' . The density of state near the Fermi level is given by

$$\rho(E) \approx \frac{2E}{\pi(\hbar v_F)^2}. \quad (2.6)$$

The vanishing density of state at zero energy makes it easy to adjust the Fermi level without altering the chemical properties of graphene, e.g., by doping with an electric field [3]. However, the gapless band structure of MLG makes it impossible to completely turn off the current flowing through the channel limiting its usage in many applications.

One of the simple ways to modify the electronic properties of graphene and other 2D materials, in general, is to create a heterostructure consisting of layers of 2D materials stacking on top of the other. Each layer of 2D materials adheres to the other with the universal van der Waals interactions. This makes it possible to assemble the

heterostructure with any combination of 2D materials regardless of their crystal structure to create a material with desire electronic properties. These kinds of structures are collectively known as van der Waals heterostructures.

The simplest graphene-based heterostructure is bilayer graphene (BLG) which consists of a stack of two MLG. However, much more exotic physics emerge when the crystal orientation of one layer of BLG is rotated respected to the other layer with a twist angle θ . This system is well-known as twisted bilayer graphene (tBLG). Figure 2.2(a, b) show the crystal structure of tBLG consisting of an alternating of bright and dark spots. The centers of bright spot regions appear when carbon atoms of the top layer are aligned directly on top of the carbon atoms of the bottom layer with the same sublattice, i. e., top layered carbon atoms in A sublattice are on bottom layered carbon atoms in A sublattice. This alignment is referred to as AA stacking. On the contrary, the centers of dark spot regions emerge when carbon atoms of the top layer are aligned directly on top of the carbon atoms of the bottom layer with different sublattice and there are carbon atoms that have no partner located at the center of the hexagonal ring of the other layer. This alignment is called AB or Bernal stacking. These bright and dark spots create a new pattern on the heterostructure called Moiré pattern. If the Moiré pattern of tBLG is periodic, the structure is said to be commensurate which usually occurs when the twist angle, θ , is small. Whereas at a large angle, the pattern is usually not periodic resembling the structure of quasicrystal [17]. This structure is said to be incommensurate.

For small twist angle tBLG, the Moiré superlattice is usually periodic forming large unit cells with periodicity depend on a twist angle θ

$$L_{\theta} = \frac{a_0}{2\sin(\theta/2)} \quad (2.7)$$

The large periodicity of the Moiré unit cell results in a small Moiré Brillouin zone (MBZ) as shown in Figure 2.2(c). The MBZ can be constructed from the parents BZ of the two MLG rotated with respect to each other with angle θ . It consists of two inequivalent hexagons located in momentum space near K and K' points of the parents BZ [18]. The size of the MBZ depends on the shift in wavevector of the two parents BZ,

$$k_{\theta} = 2G_K \sin\left(\frac{\theta}{2}\right), \quad (2.8)$$

where $G_K = \frac{4\pi}{3a_0}$ is the magnitude of the wavevector $\Gamma - K$ of MLG.

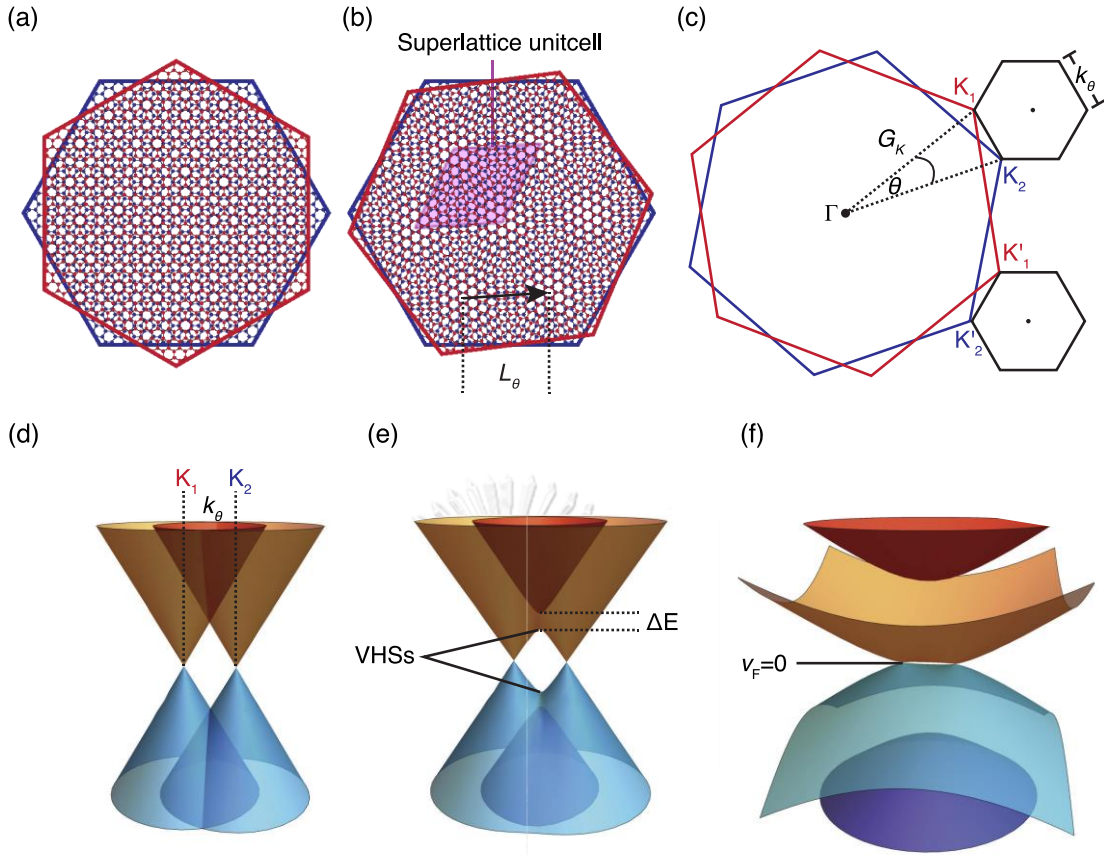


Figure 2.2(a) Crystal structure of incommensurate tBLG. The top graphene layer (red hexagon) is rotated by 30° with respect to the bottom layer (blue hexagon). (b) Crystal structure of commensurate tBLG with a twist angle $\theta=7.34^\circ$. The heterostructure has a periodic Moiré pattern with a large periodicity L_θ (c) Moiré Brillouin zones located at K and K' points of parents Brillouin zone. The size of Moiré Brillouin zones depends on a twist angle θ . (d-f) the evolution of tBLG band structure. (d) In the absence of interlayer coupling, the Dirac cones of top and bottom layers are not interacting with each other and the band structure for both layers are the same as MLG. (e) At small interlayer coupling, the conduction and valence bands of both layers are hybridized creating saddle points with a very large density of state. There is also an energy gap, ΔE , opening at the saddle points. (f) For large interlayer coupling, the conduction and valence bands become considerably flat throughout Moiré Brillouin zones, and the Dirac velocity vanishes. Figure 2.2(d-f) are adapted from Ref.[18].

The band structure of tBLG was first calculated by R. Bistritzer and A. H. MacDonald using the continuum model [19] in 2011. The continuum model describes the Hamiltonian of a single valley of tBLG at low energy. The effective Hamiltonian of tBLG near the K valley can be expressed as

$$H_{\text{tBLG}} = \begin{pmatrix} v_F \boldsymbol{\sigma} \cdot \mathbf{p}_T & T(\mathbf{r}) \\ T^\dagger(\mathbf{r}) & v_F \boldsymbol{\sigma} \cdot \mathbf{p}_B \end{pmatrix}, \quad (2.9)$$

where $v_F = \frac{1}{\hbar} |\nabla_{\mathbf{k}} E_{\mathbf{k}}|_{\mathbf{k}=\mathbf{K}, \mathbf{K}'}$ is Fermi velocity at the Dirac points, $\mathbf{p}_i = \hbar(\mathbf{k} - \mathbf{K}_i)$ and $i = T, B$ is an index for the top and bottom layer, respectively. $T(\mathbf{r})$ is the term that described the coupling between two layers generated by Moiré potential [20]. The Hamiltonian is acting on a sublattice degree of freedom for both top and bottom layers.

The coupling term, $T(\mathbf{r})$, depends sensitively on a twist angle between layers. At a large angle, the coupling strength is believed to be small due to a large momentum mismatch between two graphene layers [21] resulting in vanishing of $T(\mathbf{r})$. In this case, H_{tBLG} can be approximated to be diagonal and electronic states in top and bottom layers are decoupled. Since the diagonal terms resemble the Hamiltonian of MLG, electrons travel through the tBLG on each layer with the same behavior as that of MLG. For a small twist angle tBLG, the coupling between layers becomes relevant leading to a drastic change in the electronic properties of graphene.

The low energy bands of tBLG can be viewed as a mixing of two Dirac cones at the same valley between the two layers as shown in Figure 2.2(d-f). The hybridization of Dirac cones causes conduction and valence bands of the two MLG layers to merge to each other resulting in four energy bands near the Fermi energy. At the intersection point between two parents Dirac cones, flat dispersions are formed and an energy gap, ΔE , between the lowest energy bands and the subsequent bands is opened. This gap is referred to as a superlattice gap since it is induced by the superlattice potential of the Moiré pattern. The flat dispersions, possessing a very large density of states, arise at the energy levels known as Van Hove singularities (VHSs). As the interlayer coupling strength is increased, VHSs are pushed toward zero-energy creating narrower bandwidth of conduction and valence bands and a larger energy gap at the intersection point of two parents Dirac cone.

One of the surprising results of band structure calculation is a decrease of Fermi velocity at the Dirac points (Dirac velocity). It was predicted that the Dirac velocity decreases as a twist angle is reduced until it becomes zero at twist angle $\theta \approx 1.05^\circ$. After that, the Dirac velocity oscillates with the twist angle generating a set of angles, known as “Magic angles”, in which the Dirac velocity is vanished [19]. The series of magic angles predicted by R. Bistritzer and A. H. MacDonald were given by $\theta_{\text{magic}} \approx 1.05^\circ, 0.5^\circ, 0.35^\circ, 0.24^\circ$ and 0.2° . The vanishing of the Dirac velocity is followed by a flattening of conduction

and valence bands near the Fermi energy. The energy band flattening produces a very large number of states in a narrow bandwidth (< 10 meV). This high density of state near the zero-energy makes it promising to use magic-angle tBLG (MA-tBLG) as a platform to study strongly correlated phenomena in which the electron-electron interaction cannot be ignored.

Even though the theoretical prediction suggests that a twist angle between two graphene layers can be used to greatly modify its electronic properties, the realization of such structure becomes an issue since the electronic properties of tBLG is extremely sensitive to the twist angle. This problem was overcome by a development of the so-called “tear-and-stack” technique which enables the fabrication of twisted van der Waals heterostructure with unprecedented accuracy [22]. The details of the tear-and-stack technique will be explained in Chapter 3. One of the remarkable achievements of this technique was a demonstration of correlated insulating states in MA-tBLG at half-filling by Cao *et al.* in 2018. They have found that MA-tBLG exhibited unconventional insulating states below a temperature of 4 K in addition to the insulating states that appear when carrier density in graphene is tuned toward the superlattice gap, i. e., when the lowest energy band in MBZ was filled. The insulating states at the half-filled band cannot be explained by a free or weakly interacting electron model. This phenomenon is a result of a strongly correlated electron system owing to the flat bands of MA-tBLG. In the very same year, they also published a paper reporting the discovery of superconducting states in MA-tBLG [8]. In this report, MA-tBLG exhibited superconducting behavior with a critical temperature of up to 1.7 K when charge carriers were electrically doped slightly away from the correlated insulating state in a negative energy band. These two discoveries verify the application of tBLG as a platform to study exotic quantum phases without altering the chemical configuration of the material.

2.2 Raman spectroscopy

Even though the tear-and-stack technique can be used to fabricate tBLG with an arbitrary twist angle up to the accuracy of $\sim 0.1^\circ$, the heterostructure tends to relax into its energetic favorable configuration [23]. Graphene layers in natural graphite usually arrange themselves into AB or Bernal stacking since it is a configuration that has the lowest

energy [24]. To ensure that the structure remains twisted, Raman spectroscopy was employed in this study to characterize the configuration of graphene.

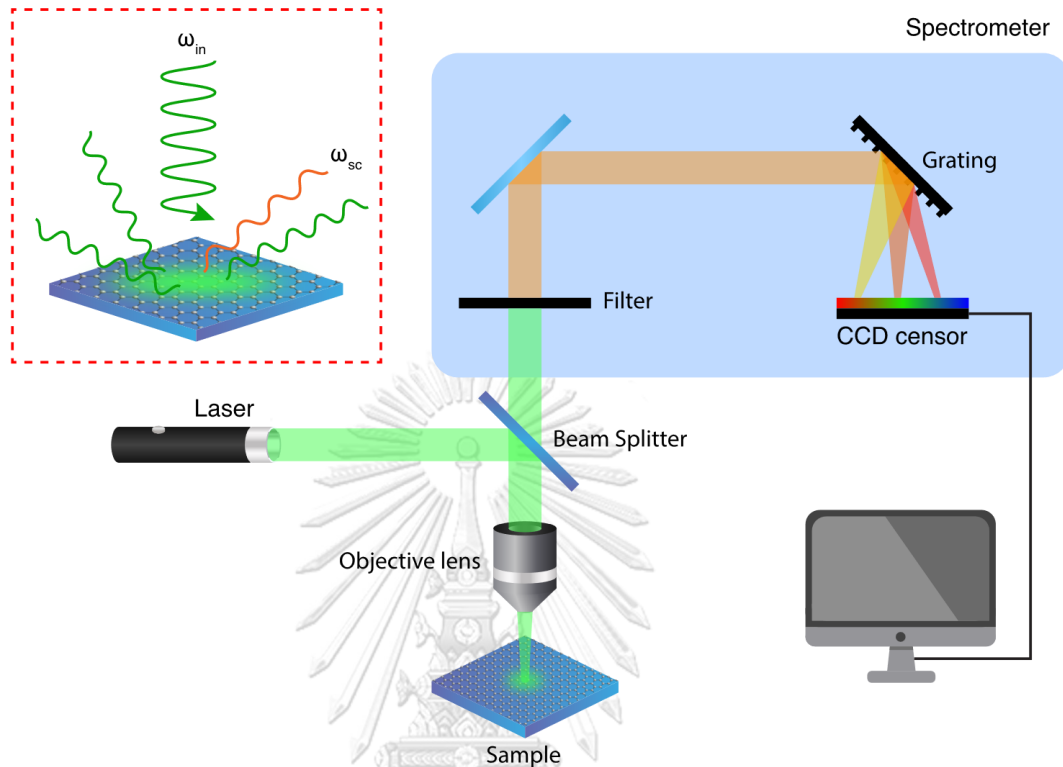


Figure 2.3 Schematic of Raman spectroscopy. The inset shows a basic diagram of a scattering mechanism of incident photons of frequency ω_{in} with a sample. The scattering photon with frequency $\omega_{sc} \neq \omega_{in}$ is depicted in the Figure by the orange wave.

A schematic of Raman spectroscopy is shown in Figure 2.3(a). Raman spectroscopy is performed by illuminating a laser of a specific frequency, ω_{in} , into a sample of interest. The sample absorbs a photon of frequency ω_{in} and then re-emits a scattering photon of frequency ω_{sc} . Usually, the frequency of the scattering photon is the same as the incident photon from the laser. However, there are a very small portion of the scattering photons that have a frequency ω_{sc} different than that of ω_{in} . We call this process Raman scattering. The photons with a frequency $\omega_{sc} = \omega_{in}$ are filtered out by a filter leaving only photons generated by the Raman process to enter the spectrometer. A grating is then used to disperse the Raman light into separate wavelengths. Finally, a CCD sensor is used to detect the intensity of the dispersed light for each wavelength. Raman spectrum is conventionally obtained by plotting the intensity of scattering light against the so-called Raman shift,

$$\text{Raman shift} = \frac{1}{\lambda_{\text{in}}} - \frac{1}{\lambda_{\text{sc}}}, \quad (2.10)$$

where λ_{in} and λ_{sc} are wavelengths of the incident and scattering photon, respectively.

The mechanism of Raman scattering can be described as follows. First, a photon of frequency ω_{in} excites the sample by creating an electron-hole (e-h) pair with energy $\hbar\omega_{\text{in}}$. The e-h pair then decays into a phonon(s), a quantization of vibrational states in crystal, with energy $\hbar\Omega$ and another e-h pair. The latter e-h pair then relaxes into the initial state by releasing a photon of frequency ω_{sc} . This process in which the frequency ω_{sc} is less than ω_{in} is called a Stokes process and it is a process that is focused in this study. Raman scattering involves scatterings of a photon with momentum $\hbar k_{\text{in}} = \hbar\omega_{\text{in}}/c$ (c is the speed of light) with phonons and electrons in a material that has certain allowed energy levels for that specific momentum. This results in a discrete set of allowed scattering frequency determined by electronic band structure and phonon dispersion relation of the material. As a result, the Raman spectrum for each material is unique so it can be used as a versatile tool to investigate the structure of the material.

Raman spectrum of pristine and defected MLG are shown in Figure 2.4(a). There are two main prominent peaks of MLG centered at around 1580 cm^{-1} and 2700 cm^{-1} . The peak at 1580 cm^{-1} is a characteristic of graphite material that arises from an interaction of an incident photon with a phonon at the Γ point [25]. This peak is well fit by a single Lorentzian function and is known as the G peak. The peak at 2700 cm^{-1} , the so-called 2D peak, originates from the interaction between electron and phonons at the vicinity of K and K' points in the momentum space [25]. Hence, this peak is sensitive to the electronic band structure of graphene and the excitation energy of the laser. Since, graphene has a band structure that evolves according to a number of layers, shapes and positions of Raman 2D peaks for different thicknesses of graphene are different as shown in Figure 2.4(c). Raman 2D peak of few-layered graphene is wider than that of MLG and can be fit with multi-peak Lorentzian function as shown in Figure 2.4(d). The dependent of Raman 2D peak on thickness of graphene can be employed to characterize a number of layers for few-layered graphene. For defected graphene, additional peaks are observed at around 1350 cm^{-1} and 2950 cm^{-1} , called D and D+D' peaks. As same as 2D peak, D and D+D' peaks are dispersive meaning that their position and shape depend on the energy excitation of the laser. The origin of this peak is defects in graphene sheet that enables

a phonon to be scattered with energy corresponding to the observed peaks [25]. Thus, the intensity of these peaks is useful for the characterization of the quality of graphene. For a high-quality graphene device, the graphene layer should be defect-free and these peaks should vanish since any kind of defects introduces potential fluctuation that hinders the transportation of electrons in the graphene channel.

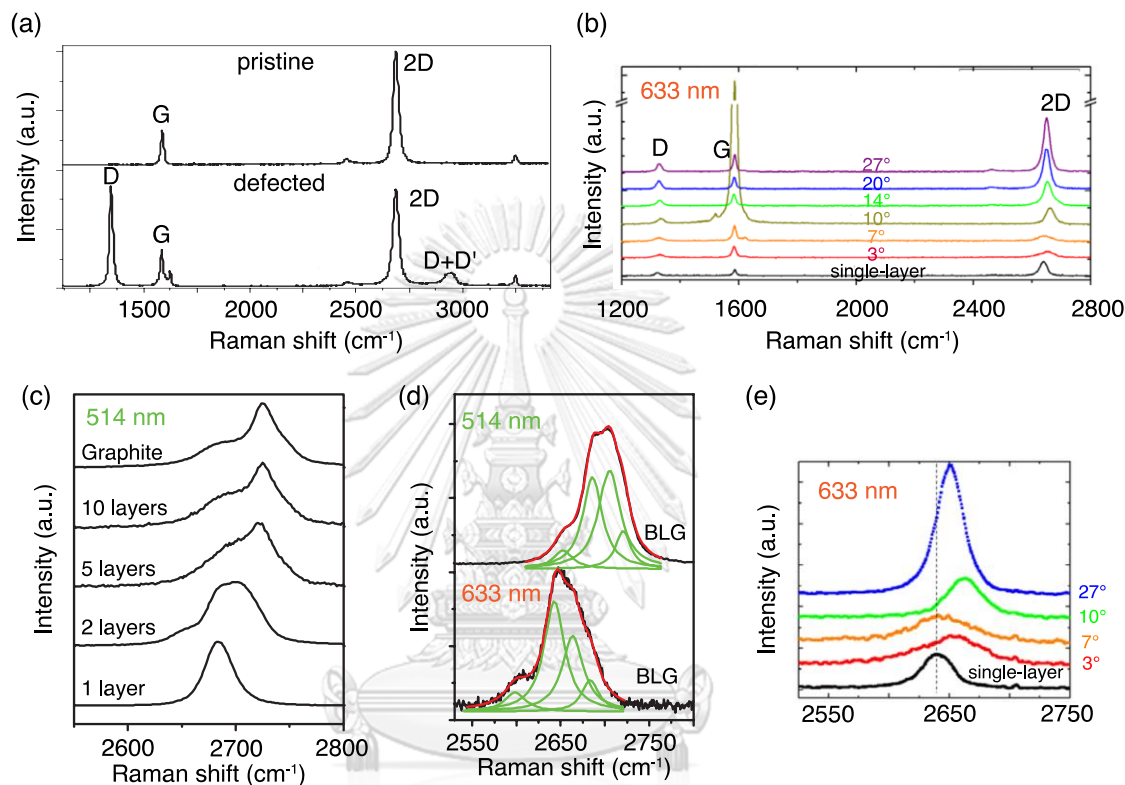


Figure 2.4(a) Raman spectrum of pristine (top) and defected (bottom) MLG. (b) Raman spectrum of MLG and twisted bilayer graphene with different twist angles obtained from chemical vapor deposition (CVD) process. The data is obtained from a laser excitation of 1.96 eV (633 nm). (c) Evolution of Raman 2D band from single layer of graphene to bulk graphite obtained from a laser excitation of 2.41 eV (514 nm). (d) Comparison between Raman 2D bands of the same BLG obtained using different laser excitations. Both spectra can be fit with multi-peak Lorentzian function shown as green lines in the Figure. (e) Evolution of tBLG Raman 2D bands with a twist angle. Figure 2.4(b, e) and 2.4(a, c, d) are adapted from Ref.[26] and Ref.[25], respectively.

For tBLG, the periodic potential introduced by the Moiré pattern activates addition Raman peaks located near the G peak observed in tBLG with a middle twist angle ($\sim 8^\circ$ - 15°). These peaks are usually followed by a massive enhancement of G peak intensity [27] as shown in Figure 2.4(b). The massive enhancement of the G peak manifests in Raman spectra when the energy of the laser is resonant with the energy gap of the two

VHSs in the density of states of tBLG. Since the positions of VHSs depend on a twist angle between two graphene layers, the resonance energy of the laser is also changed with the twist angle. Typical Raman spectroscopy uses a laser excitation with have a wavelength in the range of visible light. As a result, the massive enhancements of the G peak are only observed in tBLG with a middle twist angle.

To distinguish a small twist angle tBLG from AB-stacked BLG, one can use a shape of Raman 2D peak to characterize the stacking configuration of graphene. Since the shape of the Raman 2D peak is determined by the electronic band structure of tBLG which is sensitive to a twist angle for small twist angle tBLG, it can be used to differentiate tBLG from the AB-stacked one. For large twist angle tBLG, the Raman 2D peak of tBLG has the same shape as that of MLG and can be fit by a single Lorentzian function as shown in Figure 2.4(e). This result is in agreement with a theoretical calculation predicting that electronic properties of large twist angle tBLG should be the same as MLG due to a decoupling between two graphene layers.

2.3 Charge transportation in graphene-FET devices

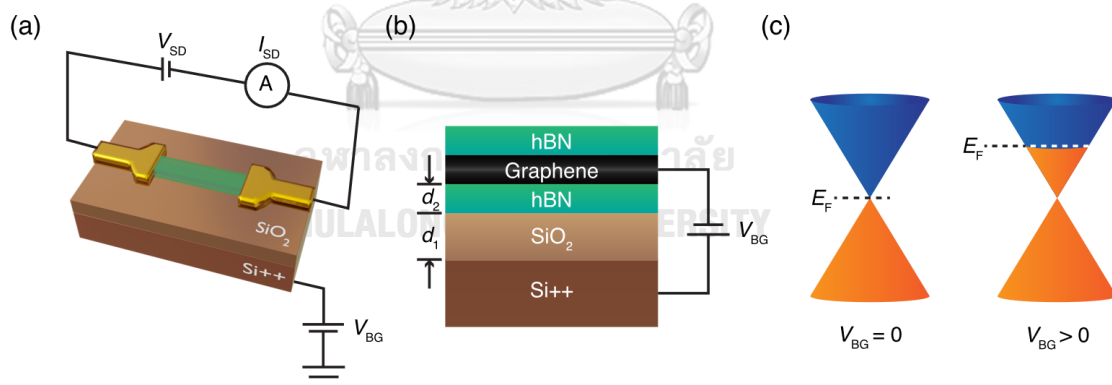


Figure 2.5(a) A basic diagram of FET using hBN-encapsulated tBLG as a transport channel. (b) A side-view image of the FET in Figure 2.5(a) demonstrating parallel-plate capacitor geometry. (c) Dirac cones at K point demonstrating a shift in Fermi energy, E_F , when V_{BG} , is applied to the silicon back gate. Filled states are shown as orange color while empty states are shown as blue color.

In this thesis, the hBN-encapsulated tBLG was built into FET as schematically demonstrated in Figure 2.5(a). The FET device was fabricated on an insulating layer of SiO_2 with a highly-doped silicon as a back gate. Charge carriers were injected and extracted by metal electrodes that were contacted to the edges of graphene. The metal

electrodes act as source and drain for the FET. By applying a source-drain voltage, V_{SD} , between source and drain electrodes and measuring source-drain current, I_{SD} , flowing through the transport channel, one can observe the electronic behavior of tBLG through macroscopic properties such as conductivity and resistivity of tBLG. Charge carrier density in tBLG can be controlled by applying a back-gate voltage, V_{BG} , to the Si as shown in Figure 2.5(a). The induced charge in the graphene channel can be understood by a parallel-plate capacitor model as demonstrated in Figure 2.5(b). In this case, graphene and Si act as metal plates separating by two dielectric layers of SiO_2 and hBN. The amount of carrier density, n , induced by V_{BG} can be determined by a relation,

$$n = \left(\frac{\epsilon_{r1}\epsilon_{r2}\epsilon_0}{e\epsilon_{r2}d_1 + e\epsilon_{r1}d_2} \right) V_{BG} = CV_{BG} \quad (2.11)$$

where e is a magnitude of electron charge, ϵ_0 is the permittivity of free space, d_1 and d_2 are thicknesses of SiO_2 and hBN, ϵ_{r1} and ϵ_{r2} are dielectric constants of SiO_2 and hBN, respectively, and C is capacitance per unit area of the system.

The V_{BG} is also directly affects Fermi energy of tBLG as shown in Figure 2.5(c). For an undoped tBLG, i.e., $V_{BG} = 0$ V, the Fermi energy lied at the Dirac point so that the valence band is filled and the conduction band is empty. Therefore, the undoped tBLG should conduct no current. If V_{BG} is tuned toward a positive value, electrons are induced into the conduction band shifting Fermi energy to a higher value as shown in Figure 2.5(c). On the contrary, electrons are removed from the valence band if V_{BG} is adjusted to be negative. This creates holes as the majority charge carriers in the transport channel shifting the Fermi energy into a negative value. The ability to freely control the amount of charge carrier density by just changing the back-gate voltage is invaluable for investigating electronic transport behavior at any given Fermi energy.

Unfortunately, the electrical current, I_{SD} , flowing through the channel does not represent the intrinsic transport properties of tBLG. This can be understood by a circuit diagram shown in Figure 2.6(a). When electrons are injected into or extracted from the channel, there will be a voltage drop in addition to the voltage drop from the resistance of tBLG. This additional resistance is referred to as “contact resistance”, which arises due to an energy mismatch between Fermi energy of electrons in metal and graphene.

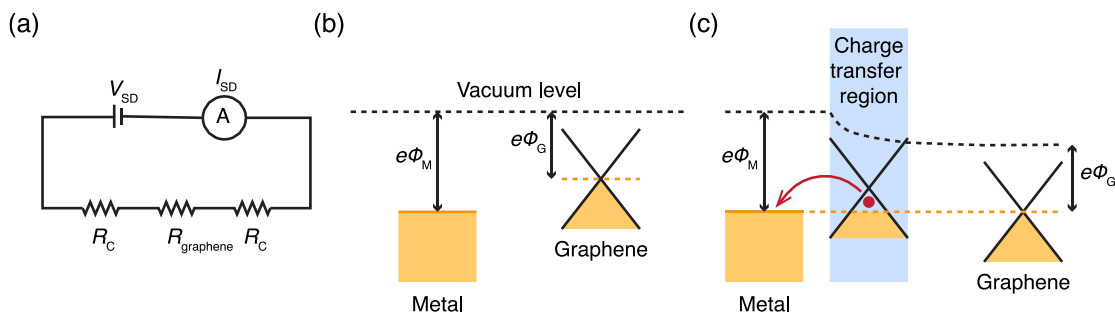


Figure 2.6(a) A circuit diagram showing contact resistances, R_C , for the FET shown in Figure 2.5(a). (b) An energy band diagram for isolated systems of metal and graphene. (c) An energy band diagram demonstrating charge transfer at the interface between metal and graphene. The shaded regions of the band structures in Figure 2.6(b, c) represent filled states of electrons up to the Fermi energy.

Another important effect of metal contact is charge transfer at the interfaces between tBLG and metal electrodes. The amount of charge transfer depends on a difference between work functions of tBLG and the metal. The work function, Φ , of a material is determined by the energy that is required to remove an electron at the Fermi energy to a point in the vacuum outside the material surface. Figure 2.6(b) shows an energy band diagram of isolated metal and graphene systems. The work functions of tBLG, Φ_G , and metal, Φ_M , relates their Fermi energy with the vacuum level. When a high work function metal is brought into intimate contact with tBLG, electrons from tBLG will be transferred to the metal to reduce their energy as illustrated in Figure 2.6(c). This creates a positive-charged region on tBLG near the contact interface. The charge transfer region may introduce a potential barrier at the contact point, hindering the transport characteristic of graphene. The amount of charge transfer can be reduced by using metal with a work function close to that of tBLG. In this study, Mo was used to make intimate contact with tBLG since its work function of 4.5 eV [13] is comparable to that of tBLG which also has a value of around 4.5 eV [28].

Chapter 3

Device Fabrication

In this chapter, I will explain about fabrication process of FET device used to investigate transport properties in this study. The chapter starts with the mechanical exfoliation of 2D materials from their bulk crystals. Then, BNGBN assembly using the tear-and-stack technique will be described. After that, details regarding deposition of Mo contact to BNGBN will be presented. The last section provides information about wire bonding, a process in which the FET device is connected to a chip carrier.

3.1 Graphene and hBN exfoliation

In this project, A blue tape BT-150P-ALC from Nitto Denko Material (Thailand) Co., Ltd. was used for exfoliation. The blue tape was selected in this study due to its acceptable adhesion force and relatively low glue residue. Graphene flakes were obtained from natural graphite. hBN flakes were obtained from bulk hBN single crystal grown under high pressure and high temperature as described in Ref. [29]. The exfoliation process started with sticking a piece of bulk crystal (graphite or hBN) to one end of a strip of the blue tape (Figure 3.1(b)). Some of the graphite or hBN flakes would be attached to the tape after the bulk crystal had been pull out (Figure 3.1(c)). The thickness of the flakes was then reduced by folding one end of the strip to the other end (Figure 3.1(d)) then peeling off. Repeating this step 4-8 times, one obtained a “mother tape” containing 2D crystal flakes spreading over the tape as shown in Figure 3.1(e).

In this thesis, a highly doped silicon wafer with thermally grown SiO_2 with a thickness of 285 nm was used as a substrate for graphene and hBN flakes. The silicon wafer was divided into rectangular pieces with a size of around 1×1 cm called “silicon chips”. The 2D crystals on the mother tape were then transferred to a silicon chip by following steps. First, another strip of the blue tape was pasted onto the mother tape then peeled off. In this step, some flakes on the mother tape would be transferred to the second tape which was referred to as “daughter tape”. Before transferring the flakes on daughter tape to a silicon chip, the surface of the chip was cleaned by oxygen plasma

using a radio frequency (RF) plasma generator (300 W, 50 Hz) to remove ambient adsorbates on Si/SiO₂ substrate. The plasma cleaning process was performed at a pressure of 150 mTorr for 300 s. After the cleaning process, the daughter tape was brought into contact with the cleaned silicon chip as shown in Figure 3.1(f). In the last step, the chip along with the daughter tape were heated on a hot plate at a temperature of 100°C for 2 minutes before peeling the tape from the substrate when it had been cooled down to room temperature. A combination of surface cleaning and substrate heating promotes an increase in a uniform contact area between the interfaces of Si/SiO₂ substrate and the tape, resulting in a larger size of 2D material flakes [30].

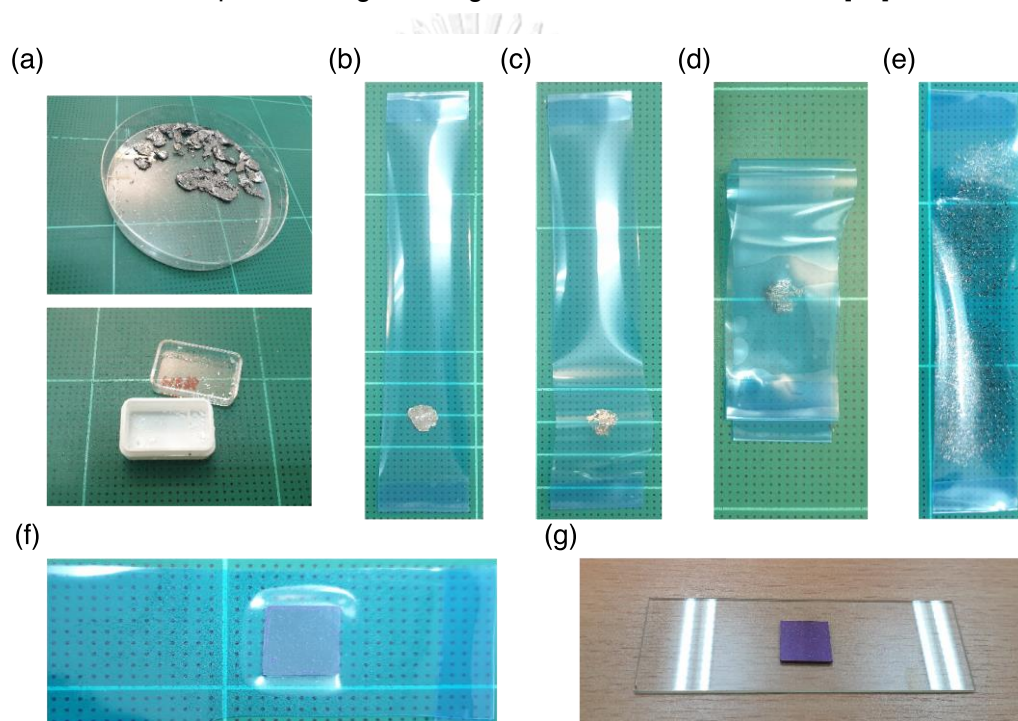


Figure 3.1(a) Natural graphite (top) and bulk hBN single crystals (bottom). Figure (b-f) illustrate mechanical exfoliation process demonstrating a cleavage of graphene flakes from graphite. (g) A silicon chip after exfoliation process containing graphene flakes on its surface.

3.2 2D material flakes identification

After preparing graphene and hBN flakes on silicon chips, optical microscope was then used to select suitable flakes for device fabrication. Figure 3.2(a, b) shows optical images of exfoliated graphene and hBN flakes on Si/SiO₂ substrates. MLG and hBN flakes which size larger than 20×20 μm were selected to create BNGBN.

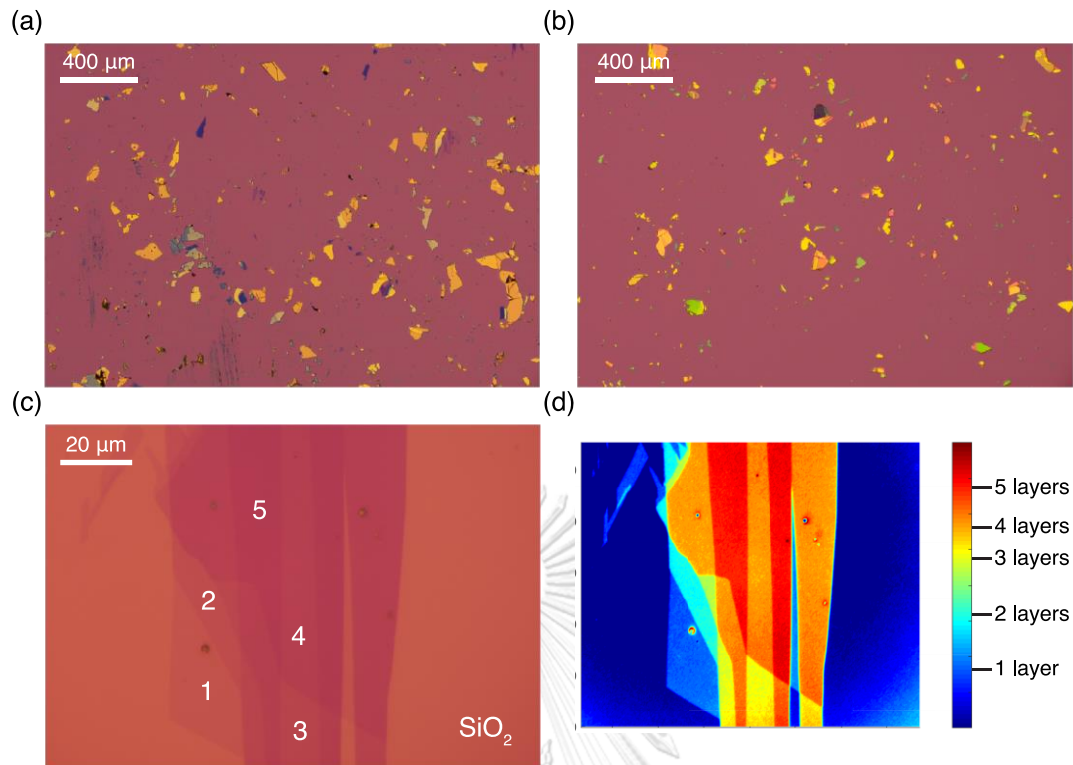


Figure 3.2 Optical images of (a) graphene and (b) hBN flakes on Si/SiO₂. (c) Optical image of few-layer graphene showing different color contrast for graphene with different thicknesses. The numbered labels indicate the number of graphene layers. (d) Image plot of C value for optical image in Figure 3.2(c). The color scale is ranged from 0.0-0.4.

Thicknesses of graphene flakes can be estimated by the contrast of graphene compared to Si/SiO₂ substrate as shown in Figure 3.2(c). The numbers 1-5 in Figure 3.2(c) indicate the number of graphene layers for each region in the image. A single layer of graphene was found to absorb incident white light of approximately 2.3% [31] resulting in its high transparency. An amount of reflected light from graphene was predicted to be depended on the thickness of graphene, substrate and wavelength of incident light [32]. For exfoliated graphene on Si/SiO₂ substrate with the SiO₂ thickness of 285 nm, the thickness of graphene can be determined by the contrast spectrum,

$$C(\lambda) = \frac{R_{\text{sub}}(\lambda) - R_{\text{graphene}}(\lambda)}{R_{\text{graphene}}(\lambda)}, \quad (3.1)$$

where λ is reflected light intensity, $R_{\text{sub}}(\lambda)$ and $R_{\text{graphene}}(\lambda)$ are reflected light intensity coming from Si/SiO₂ substrate and graphene on Si/SiO₂, respectively. Based on the Fresnel equation, The contrast value yields the highest amount for the reflected light in the range of a green light spectrum [32]. The contrast value was also predicted to be

depended linearly on the thickness of graphene. In this thesis, RGB values for each pixel in the optical image of graphene were used to estimate the average intensity of reflected light in the range of red, green and blue spectrum. The contrast value in the green light spectrum calculated by

$$C = \frac{G_{\text{sub}} - G_{\text{graphene}}}{G_{\text{graphene}}}, \quad (3.2)$$

where G_{sub} and G_{graphene} are G value obtained from the optical image in the region of Si/SiO₂ substrate and graphene, is then used to determine the thickness of graphene. Figure 3.2(d) plots the values of C for each pixel of the image in Figure 3.2(c) where clearly difference in C value for graphene with different thicknesses can be used to determine the number of graphene layers. An MLG flake is then selected to form tBLG.

Thicknesses of hBN manifest through the color of hBN flakes in the optical images owing to the thin-film interference. Suitable hBN flakes for device fabrication have thicknesses of around 20-40 nm which appear in optical images as green color. The color-dependent thickness of hBN is confirmed by atomic force microscopy (AFM) as shown in Figure 3.3(e). hBN flakes with a light green color, such as the flake shown in Figure 3.3(d), have a thickness of around 40 nm. Thinner hBN flakes such as the flakes shown in Figure 3.3(a-c) appear as darker green color. Suitable two hBN flakes are then selected to create tBLG via the tear-and-stack technique which will be explained in the next section.

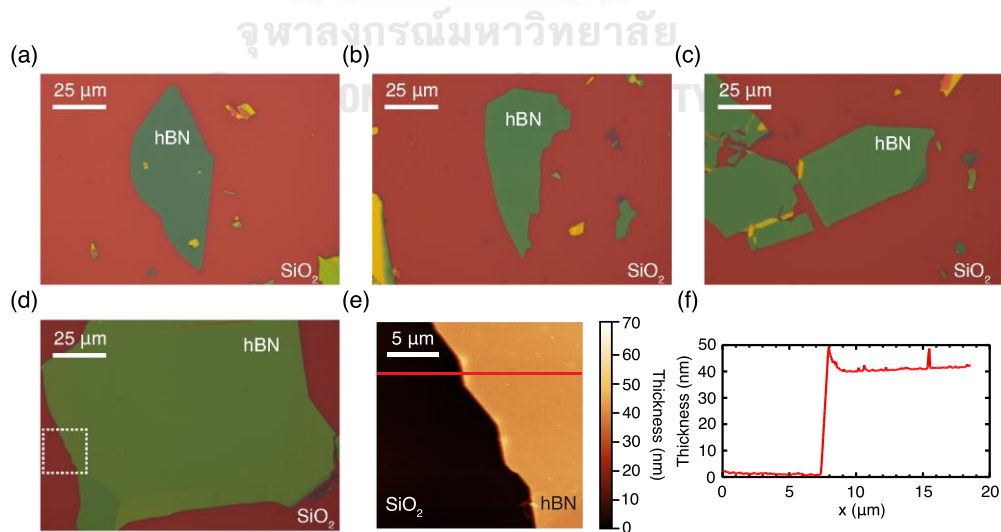


Figure 3.3(a-d) Optical images of suitable hBN flakes. (e) False color image of hBN obtained from AFM in the region within the dash line of Figure 3.3(d). (f) Thickness profile extracted from the red line in Figure 3.3(e) showing hBN thickness of around 40 nm.

3.3 BNGBN assembly

To encapsulate tBLG by two hBN sheets, the selected MLG and hBN flakes need to be transferred onto another silicon chip and stacked on top of each other to create a sandwich structure. In this study, a polymer stack of poly(bisphenol A carbonate) (PC) film on a block of Polydimethylsiloxane (PDMS) was used to pick up and transfer the selected flakes onto a desired substrate. This polymer stack was referred to as a “stamp”. A twisted structure of graphene was created using the tear-and-stack technique in which hBN flake was used to tear an MLG flake into two parts and each part of MLG was then stacked together with a relative twist angle.

3.3.1 Stamp preparation

A PC solution was prepared by dissolving PC in chloroform with a concentration of 6% by weight. PDMS block was prepared by mixing PDMS with curing agent with a weight ratio of 10:1 in a Petri dish. The Petri dish was then kept in a vacuum desiccator until PDMS was solidified.

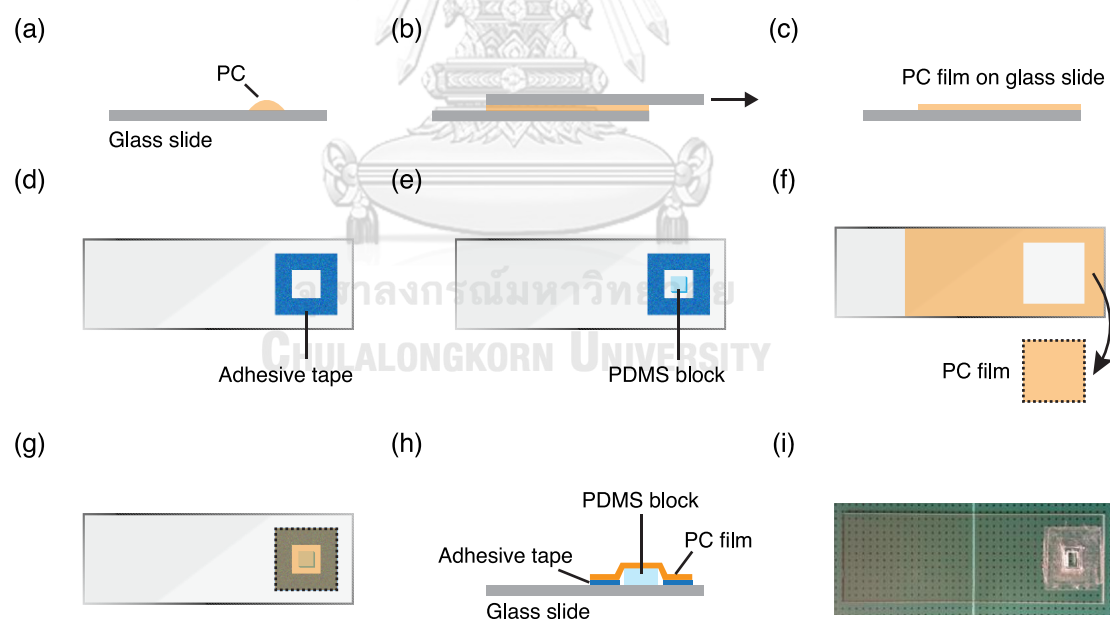


Figure 3.4(a-g) Side view images illustrating stamp preparation on a glass slide. (a) PC solution is dropped onto a glass slide then (b) another glass slide is immediately used to spread out PC solution. (c) PC film is formed on a glass slide after chloroform has been evaporated from PC. (d, e) PDMS block is prepared on a separate glass slide then (f) a part of PC film from the first glass slide is transfer

to (g) stack with the PDMS block. (h) Side view image of a polymer stack of PC on PDMS. (i) Image of a fabricated PC/PDMS stamp.

PC film was prepared by dropping PC solution onto a clean glass slide (typically 3-4 drops using 3 ml plastic pipette) as shown in Figure 3.4 (a). Another glass slide was then immediately used to sandwich and spread out PC solution over a glass slide (Figure 3.4(b)). After waiting around 20 minutes, chloroform would have been evaporated leaving a thin film of PC on the glass slide (Figure 3.4(c)). Double-sided tape with a rectangular hole was stuck to another separate glass slide for polymer stacking preparation (Figure 3.4(d)). A cutter knife was used to divide the solidified PDMS, which is a transparent elastomer, into blocks where each PDMS block has a size of around 3×3×1 mm. After that, a PDMS block was put onto a prepared glass slide in the center of the hole of adhesive tape as shown in Figure 3.4(e). A part of prepared PC film with a size of around 1.5×1.5 cm was cut from its original slide (Figure 3.4(f)). The rectangular PC film was placed on top of the prepared PDMS block as shown in Figure 3.4(g) and stuck to the glass slide by the adhesive tape. Figure 3.4(f) shows an example of a PC/PDMS stamp created during a fabrication process.

3.3.2 Tear-and-stack technique

Figure 3.5(a) shows an experimental setup for BNGBN assembly. The assembly process was performed under a modified microscope with a temperature-controlled stage. A PC/PDMS stamp was attached to a clamp that can be moved freely in x-, y- and z- directions using a micromanipulator as shown in Figure 3.5(b). A Si/SiO₂ substrate that contains selected graphene or hBN flakes was put onto the center of the stage. A vacuum pump was connected to the center of the stage via pump tubing to hold substrate with the stage. This is to make sure that there is no relative movement between the substrate and the stage during the transfer process. The stage can be moved in x and y directions using a micromanipulator and rotated around z-direction using a rotation manipulator as shown in Figure 3.5(b). It was also connected to a thermocouple to control the temperature of the stage. All the assembling process was displayed on a monitor which connected to a CCD camera of the optical microscope.

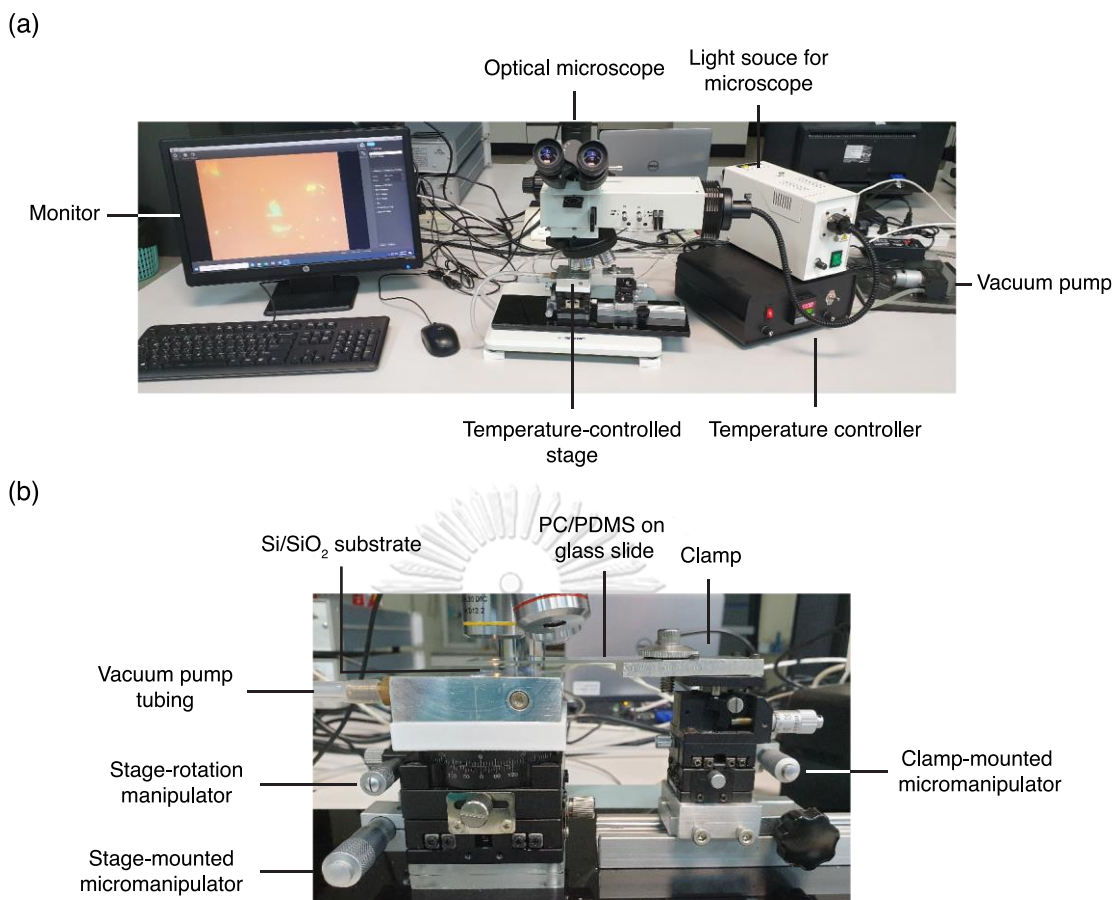


Figure 3.5(a) An experimental setup for BNGBN assembly. (b) A zoom-in image of the transfer station containing a temperature-controlled stage and a clamp used to control a movement of stamp.

Figure 3.6(a-c) shows examples of suitable MLG and hBN flakes used for creating BNGBN in this study. The assembly process started by putting Si/SiO₂ substrate that contained the selected hBN flake onto the transfer stage. This hBN would be the top layer of the BNGBN heterostructure. A prepared PC/PDMS stamp was attached to the clamp and aligned over the selected hBN flake using micromanipulators. The temperature controller was used to adjust the stage temperature to 100°C to promote adhesion between the hBN flake and the PC film. The clamp-mounted micromanipulator was then used to lower down the PC/PDMS stamp until the PC film made contact with Si/SiO₂ substrate. The contact between PC film and SiO₂ created a line separating PC film between a region that made contact with SiO₂ and a region that had not made contact with the substrate. This line would be referred to as a contact front. The stamp was then gradually lowered to slowly move the contact front until the contact front was moved pass through the hBN flake as shown in Figure 3.6(d). After waiting for 1 minute, the stamp

was slowly raised up from the substrate and the hBN flake would be picked up by the stamp as shown in Figure 3.6(e).

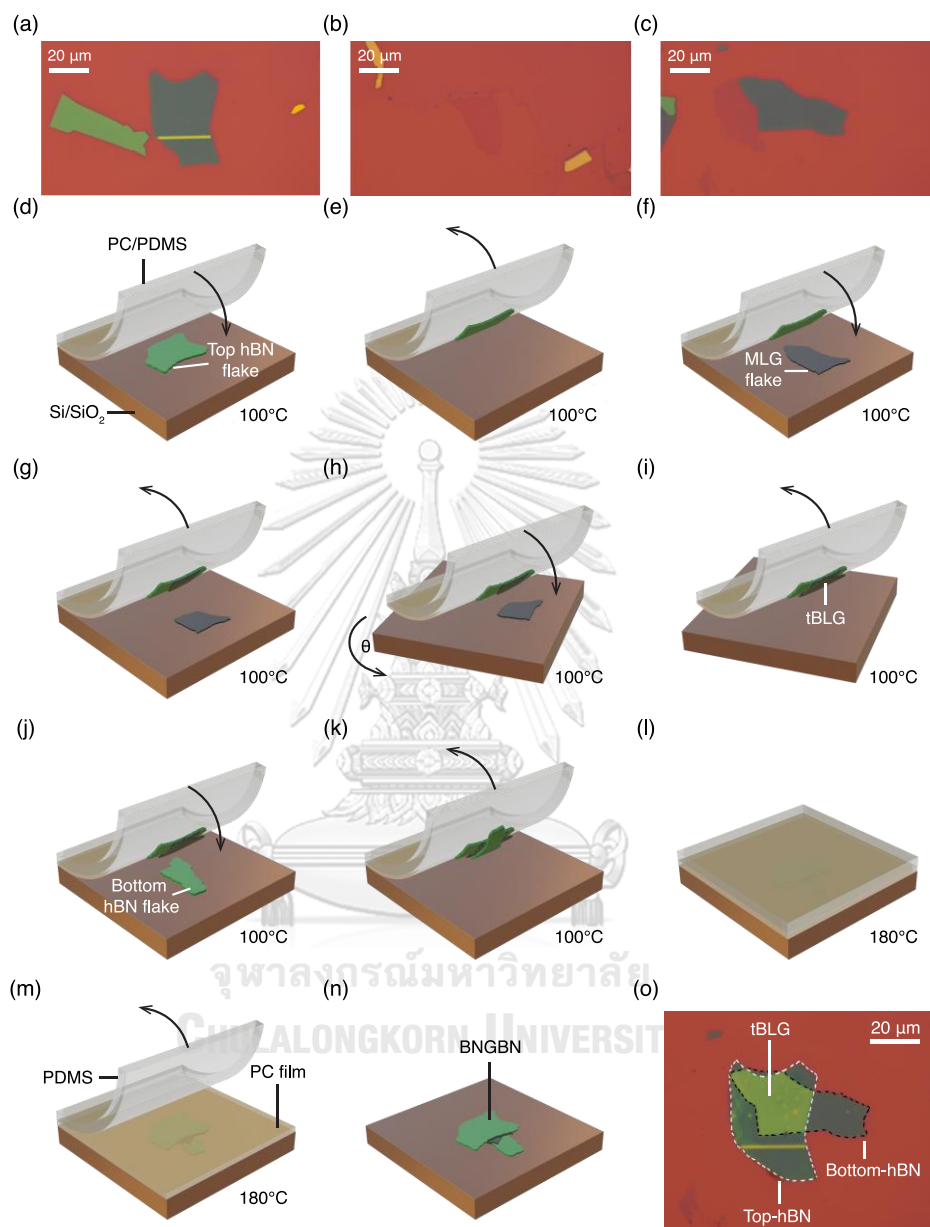


Figure 3.6(a-c) Optical images of selected 2D material flakes used as (a) top-hBN, (b) graphene and (c) bottom-hBN. (d-n) Schematics illustrating BNGBN assembly described in subsection 3.3.2. The rotation angle, θ , in Figure 3.6(h) is exaggerated for clarity. (o) Optical image of BNGBN after the transfer process. Top- and bottom-hBN are enclosed within white and black dash lines, respectively. A tBLG is formed in the overlapping region between top- and bottom-hBN.

A tBLG was created from a single flake of MLG by the following steps. First, the selected MLG flake was put on the center of the transfer stage at 100°C and the stamp

was aligned to MLG in such a way that the picked-up hBN on the PC film was covering only some parts of MLG flake. After that, the pick-up technique was performed on the MLG flake just like the hBN picking process (Figure 3.6(f)). However, only a part of MLG that had been covering by hBN was picked up in this process as depicted in Figure 3.6(g). This process tore the MLG flake into two parts: one part remained on Si/SiO₂ and the other part was picked up with top-hBN. This happened due to the stronger adhesion force between graphene and SiO₂ compared to that of PC film. After that, the stage was rotated by ~1.1° around the z-axis which is the first magic angle of tBLG as demonstrated in Figure 3.6(h). The part of MLG on the stamp was then aligned over the other part on Si/SiO₂ to pick the remaining part on the substrate to the stamp as shown in Figure 3.6(i). This process created tBLG on hBN/PC/PDMS with a twist angle equal to the angle of stage rotation during the process shown in Figure 3.6(h). To encapsulate tBLG, the Si/SiO₂ substrate with the prepared bottom-hBN flakes was placed on the stage (Figure 3.6(j)) then the bottom-hBN flake was picked up by the stamp creating BNGBN heterostructure on the PC film as illustrated in Figure 3.6(k).

During BNGBN assembly process, adsorbates on graphene, hBN and SiO₂ surface may be trapped between layered interfaces within BNGBN [33]. These contaminants appear as “blisters” in the heterostructure which greatly hinder the electronic transport properties of tBLG. To remove the blisters from BNGBN, A plasma-cleaned Si/SiO₂ substrate was prepared as a new substrate for BNGBN. The new silicon chip was heated up to 180°C by the temperature-controlled stage. The BNGBN on PC/PDMS was then transferred onto a new substrate by gradually lowering them down toward Si/SiO₂ until most parts of the PC/PDMS made contact with the substrate as demonstrated in Figure 3.6(l). During the contact front was advancing across BNGBN at 180°C, the trapped contaminants would be energetic enough to be moved along with the contact front and accumulated together at the edge of the heterostructure. The interface cleaning process created blister-free regions in BNGBN which were large enough for fabricating FET devices. Since the interface cleaning process was performed at a temperature higher than the glass transition temperature of PC ($T_g=150^\circ\text{C}$), the PC film was transformed from a hard solid into a soft viscous state and torn apart from the PDMS block. After waiting the PC film to be heated up for 5 minutes, the PDMS block was lifted from Si/SiO₂. In this step, the PC film was laminated from the PDMS block, leaving it on the Si/SiO₂

substrate as illustrated in Figure 3.6(m). To remove the remaining PC film from the substrate, the entire silicon chip was immersed into chloroform for 30 minutes to dissolve the PC film. The chip was then soaked in acetone following by isopropyl alcohol (IPA) for 1 minute each to clean contaminants and residue on the substrate surface. Finally, a nitrogen gun was used to blow-drying the substrate with N_2 gas. The BNGBN obtained after the assembly process is shown in Figure 3.6(n). Figure 3.6(o) shows an optical image of BNGBN creating by the tear-and-stack technique where the heterostructure is formed at the overlapping region between top- and bottom-hBN (the light green region in Figure 3.6(l)). The yellow dots that appeared on the BNGBN are remaining blisters trapped at the heterostructure interfaces.

3.3.3 Raman spectroscopy

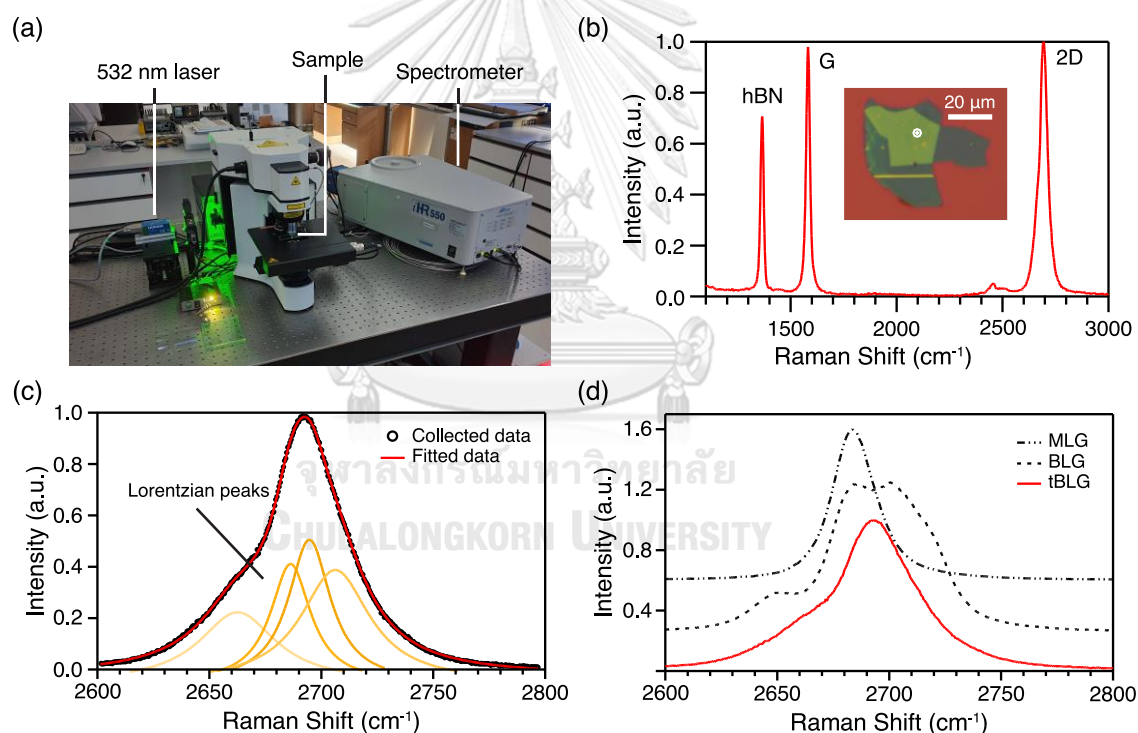


Figure 3.7 (a) Horiba IHR550 spectrometer with 532 nm laser used for Raman spectroscopy (b) Raman spectrum in the spectral range of 1100-3000 cm^{-1} . The inset shows an optical image of the BNGBN on Si/SiO₂ substrate with a circle indicating the position of the laser illuminated on the BNGBN. (c) Raman 2d peak of the BNGBN in the stacked graphene region fitted with four-peak Lorentzian (d) Comparison between Raman 2D peak of graphene for MLG, Bernal-stacked BLG and tBLG. The Raman spectra are vertically offset for clarity.

BNGBN assembly process involved heating the substrate at 180°C. This high temperature may cause a relaxation of tBLG into a Bernal-stacked configuration [23]. To ensure that the two MLG layers still preserve their twist angle, Raman spectroscopy was utilized to investigate their stacking configuration. Here, Raman spectroscopy (Horiba IHR550) with a laser excitation of 532 nm shown in Figure 3.7(a) was employed to characterize the BNGBN. The excitation laser was focused onto the BNGBN in the region that consists of a stacking of hBN/MLG/MLG/hBN which is shown as a white circle in the inset of Figure 3.7(b). A normalized Raman spectrum of the stacked graphene region is shown in Figure 3.7(b). The Raman data were obtained by illuminating the stacked graphene region with a laser (power output=50 mW) for 10 s. A 600-g/mm grating was used to disperse the Raman signal onto a CCD detector. There were a few prominent peaks in the spectral range of 1100-3000 cm^{-1} . The first two peaks that appeared at 1365 cm^{-1} and 1582 cm^{-1} are characteristic of in-plane vibration of hBN and graphene, respectively [34]. The third peak centered at 2700 cm^{-1} is a 2D peak that is sensitive to the electronic band structure of graphene. The lack of D and D+D' peaks in the Raman spectra indicates that both graphene layers are pristine, i.e., they are defect-free.

To investigate the stacking configuration of graphene sheets, Raman spectroscopy was performed with 1800-g/mm grating to increase the resolution of the Raman signal. Figure 3.7(d) shows Raman 2D peaks obtained from the stacked graphene region (solid red line, tBLG) and a region in the BNGBN that contains only a single layer of MLG (dash line, MLG). The data were collected by illuminating the laser on regions of interest for 30 s and averaging the Raman signal over three times. The Raman spectrum for the non-stacked region exhibits a single Lorentzian peak, confirming that the original graphene flake is MLG. The 2D peak on the stacked region, however, exhibits a shape that is significantly different than that of Bernal-stacked BLG as shown in Figure 3.7(d). The 2D peak of the stacked graphene region can be fitted with four-peak Lorentzian as shown in Figure 3.7(c). Since the shape of the Raman 2D peak depends on the electronic band structure of graphene, the stacked graphene region must have a different stacking configuration than that of BLG. This implies that the fabricated tBLG still retained its twist angle even after it had been heated at 180°C in the layer assembly process.

3.4 Electron-beam lithography

Electron-beam lithography (EBL) is a technique for writing down a predetermined pattern onto electron-sensitive film, called resist. An electron beam is accelerated by applying voltage and focused onto the resist to change its dissolving properties. After that, the exposed resist will be dissolved in a specific solvent, called developer, to create a designed pattern on the thin film. This type of resist is called positive-tone resist. A negative-tone resist has the opposite behavior in which only non-exposed parts of the film are dissolved in the developer. EBL is useful for creating a pattern with nanometer-sized features. The created pattern can be transferred onto an actual device by plasma etching or thin-film deposition which will be explained in the next two sections.

3.4.1 Resist spinning

In this thesis, Poly(methyl methacrylate), also known as PMMA, was used as a positive-tone EBL resist. PMMA films with two different molecular weights, 600K and 950K, were deposited onto Si/SiO₂ substrate by spin coating technique. A spin coater with a vacuum chuck is used to form bilayer resist on the substrate. PMMA (600K), which is more sensitive to electron beam than PMMA (950K), was used as a bottom layer resist. Whereas PMMA (950K) was used as a top layer. A recipe for spinning PMMA bilayer resist is described as follows

- 1) Bake the Si/SiO₂ substrate on a hot plate at 180°C for 5 minutes to remove water and adsorbed molecules from the substrate surface.
- 2) Immediately place the substrate on a vacuum chuck after substrate baking and turn on a vacuum pump. Then use a 3 ml plastic pipette to drop PMMA, 600K (1-2 drops) onto the substrate. After that, the spin coater is used to spin the substrate at 500 RPM for 5 s and speed up to 4000 RPM for 60 s to spread PMMA uniformly across the substrate surface as schematically depicted in Figure 3.8(a).
- 3) Bake the substrate on a hot plate at 180°C for 5 minutes to evaporate solvent from PMMA.
- 4) Immediately place the substrate on a vacuum chuck after substrate baking and turn on a vacuum pump. Then use a 3 ml plastic pipette to drop PMMA, 950K (1-2 drops) onto the substrate. After that, the spin coater is used to spin the

substrate at 500 RPM for 5 s and speed up to 6000 RPM for 60 s to spread PMMA uniformly across the substrate surface as schematically depicted in Figure 3.8(b).

- 5) Bake the substrate on a hot plate at 180°C for 5 minutes to evaporate solvent from PMMA. After the baking process, PMMA bilayer resist will be formed on the Si/SiO₂ substrate as illustrated in Figure 3.8(c).

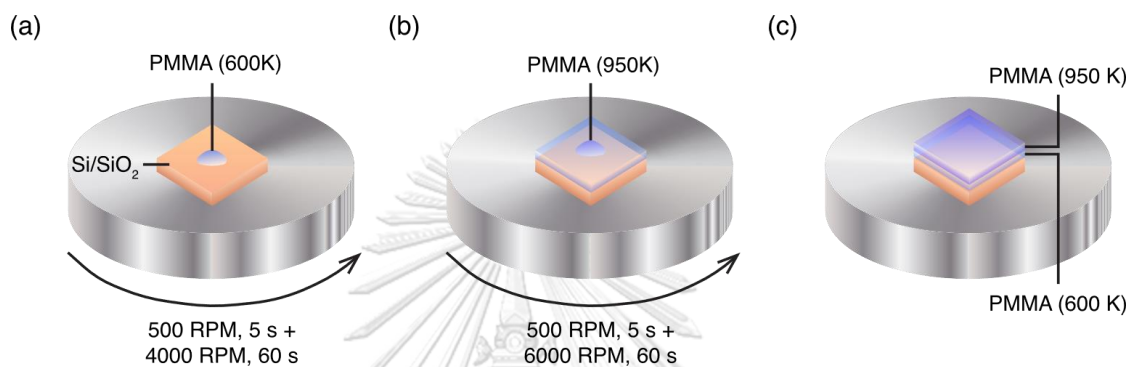


Figure 3.8 Schematics of PMMA bilayer resist spinning. (a) PMMA (600K) is dropped onto a baked substrate and spun at 500 RPM for 5 s following by fast spinning at 4000 RPM for 60 s. (b) PMMA (950K) is dropped on top of PMMA (600K) film after baking following by spinning at 500 RPM and 6000 RPM for 5 s and 60 s, respectively. (c) After baking at 180°C for 5 minutes, PMMA bilayer resist is formed on Si/SiO₂ substrate.

3.4.2 Electron-beam exposure and resist development

Even though the encapsulated structure of the BNGBN can protect graphene layers from external impurities, it imposes a problem for making electrical contact since hBN layer obstructs metal electrode to make contact with graphene. To solve this problem, The BNGBN was shaped into a rectangular structure by removing BNGBN outside the predefined rectangular shape to expose the edge of graphene. To achieve this goal, EBL was employed to define a rectangular shape on the BNGBN.

The process started by spinning PMMA resist onto a silicon chip containing the BNGBN as shown in Figure 3.9(a). In this thesis, DesignCAD It 2000, a computer-aided design software, was used to design patterns used for EBL as shown in Figure 3.9(b). The patterns were designed in such a way that most of the PMMA region on the BNGBN would be exposed to electron beam leaving two blister-free rectangular shape regions to be unexposed. These two rectangular regions of BNGBN underneath the non-exposed

PMMA would be used to fabricate FET by contacting the exposed edge of tBLG to Mo electrodes. A scanning electron microscope (JEOL, JSM-7001F) integrated with beam deflectors shown in Figure 3.9(d) was employed to focus electron beam on the sample. After the substrate had been loaded into a sample chamber, air molecules were pumped out of the chamber. When the chamber pressure was less than 3.6×10^{-4} Pa, A voltage of 30.0 kV was applied to an electron source to emit electron beam to the sample with a beam current of around 1.15 nA. The beam deflectors, controlled by computer software, were used to control the direction of the electron beam. The predefined pattern was then written down onto the PMMA resist by exposing with electron beam based on the designed pattern. The appropriate amount of electric charge per unit area radiated on the resist, known as “area dose”, was determined by the size of the smallest feature in the pattern, i.e., $500 \mu\text{C}/\text{cm}^2$ for the pattern shown in Figure 3.9(b). After a point on the substrate had been exposed to a designated number of electrons, the beam deflectors deflected the electron beam to radiate another point until the pattern was complete. The resolution for beam deflectors to move electron beam between two points, referred to as “area step size”, depends on the smallest feature size of the pattern and area dose. The pattern in Figure 3.9(b) was written with a beam step size of 16.0 nm.

The exposed regions of PMMA were then dissolved by a developer. Here, a mixing of deionized (DI) water and IPA with a ratio of 1:3 was prepared in a beaker to be used as a developer. A development process was performed at low temperature by dipping the beaker, containing the developer, into an ice bath as shown in Figure 3.9(e). After developer temperature had reached its equilibrium, the electron-beam exposed silicon chip was immersed in the developer for 60 s. The chip is then immediately transferred into a prepared IPA beaker and soaked in IPA for 60 s to clean dissolved PMMA residue. Finally, the chip was blown dry with a nitrogen gun to remove IPA and microscopic dust on the chip surface. Figure 3.9(c) shows an optical image of the developed pattern, designed as in Figure 3.9(b). The exposed region of PMMA was removed away by the developer leaving two small rectangular-shaped resist sheets on the BNGBN as shown in the dashed line in Figure 3.9(c). The remaining resists would act as etch masks in plasma etching process which will be described in the next section.

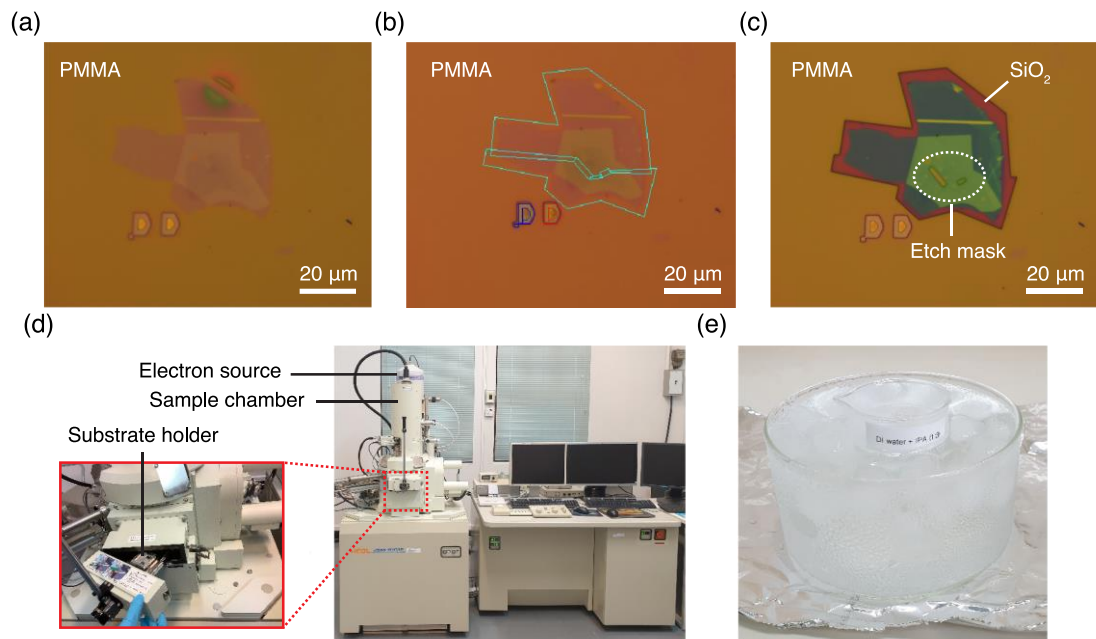


Figure 3.9(a) Optical image of BNGBN coated with PMMA bilayer resist. (b) A predefined pattern created with DesignCAD software. (c) Optical image of the BNGBN after development where PMMA region that had been exposed by electron beam was dissolved in a developer. The alphabet DD at the lower left of BNGBN is a marker that was deposited onto Si/SiO₂ substrate to use as a coordinate. (d) The scanning electron microscope, JEOL JSM-7001F, used for EBL. (e) DI water/IPA beaker dipped in an ice bath for low-temperature development.

3.5 Plasma Etching

Plasma etching is a practice used in nanofabrication to remove semiconductor materials on a substrate. A plasma generator generates a strong electric field to ionize gas molecules in the plasma chamber. The motion of ionized particles, also known as etch species, is controlled by the direction of the electric field. The electric field is used to bombard etch species onto a substrate surface removing target materials on the substrate. To selectively etch some specific regions of the substrate, a thin film polymer, called etch mask, is employed to protect any materials underneath the mask from etch species.

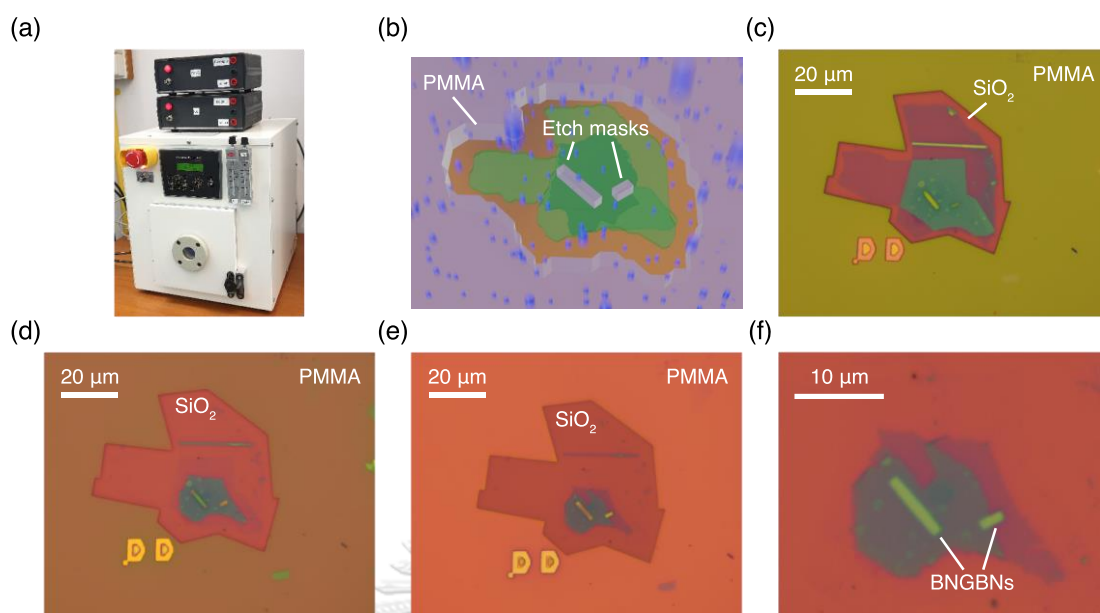


Figure 3.10(a) Plasma Etch, Inc. PE-25. Two electronic boxes above the plasma etcher are connected to mass flow controllers, used to control flow rates of O_2 and CHF_3 . (b) A schematic of the plasma etching process. O_2/CHF_3 plasma, represented by blue particles, is bombarded onto a substrate surface. (c-e) Optical images of the BNGBN after each step of etching described in section 3.5. The change in PMMA color indicates a change in thickness of PMMA after etching (f) Optical image of BNGBN after PMMA removal. The dark green layer beneath the BNGBN is a remaining part of the bottom-hBN persistent after the etching process.

In this thesis, the PMMA bilayer resist patterning by EBL was used as etch masks for BNGBN. The plasma generator used for substrate cleaning shown in Figure 3.10(a), Plasma Etch, Inc. PE-25, was also employed to etch away the part of BNGBN outside of the etch masks. A schematic of plasma etching can be seen in Figure 3.10(b). Here, O_2 and CHF_3 were used as etch species where O_2 gas has flowed into the plasma chamber until chamber pressure reached 150 mTorr then CHF_3 gas was mixed with O_2 in the chamber until the total pressure reached 300 mTorr. The chamber pressure depends on flow rates of both gas species, which were controlled by mass flow controllers. The plasma etcher was operated at power 300 W and RF frequency 50 Hz.

In this study, etch rate of hBN flakes was found to be nonlinear with time making it difficult to estimate the right amount of time used to etch away the top-hBN sheet and graphene layers. Instead of exposing the substrate to the plasma with a fixed amount of time, the etching process was divided into small sessions where each session was performed with a relatively small amount of time until the top-hBN and graphene layers

were completely etched away. The optical image of BNGBN was taken each time after the process had been complete to check if the top-hBN and graphene were completely etched. Figure 3.10(c) shows the result after the BNGBN had been etched in O_2/CHF_3 plasma for 5 minutes where the hBN flakes can still be seen through the optical microscope. Another round of plasma etching was performed for 10 minutes with the result shown in Figure 3.10(d). In this step, the non-stacked region of both top- and bottom-hBN flakes cannot be seen in the optical image. The remaining parts of hBN shown in Figure 3.10(d) are bottom-hBN that was protected from plasma by graphene layers. During the plasma process, the PMMA etch masks were also bombarded by O_2/CHF_3 plasma making it thinner every time plasma etching was performed. The change in PMMA thickness manifested in the color of its optical image due to thin-film interference. To make sure that the graphene layers outside the etch masks were completely gone, the last step of plasma etching was performed. In the last step, the BNGBN was etched in pure O_2 plasma (150 mTorr) for 1 minute following by O_2/CHF_3 plasma (300 mTorr) for 5 minutes. The final result is shown in Figure 3.10(e). To remove the remaining PMMA, the silicon chip was immersed in acetone overnight. The chip was then soaked in IPA for 1 minute to clean the remaining residue on the substrate following by blow-drying with a nitrogen gun. After plasma etching had been complete, two rectangular-shaped BNGBNs with exposed graphene edges were obtained as shown in Figure 3.10(f).

3.6 Molybdenum deposition

3.6.1 EBL for writing contacts patterns

To make contacts between Mo and tBLG, EBL was employed to write down contact patterns onto the substrate. PMMA bilayer resist was spun onto the substrate of the BNGBNs as described in subsection 3.4.1. The patterns written on the substrate can be classified into two groups: fine-featured pattern shown in Figure 3.11(a) and coarse-featured pattern shown in Figure 3.11(b). The fine-featured patterns contain structures that have sizes of less than $1 \mu\text{m}$ while the coarse-featured patterns consist of structures with larger sizes. The fine features require a lower dose than that of coarse features to increase the writing resolution for submicron-sized structures. The coarse features can be written with lower resolution for time efficiency. The fine and coarse features were

written down separately onto the substrate with different EBL parameters. The EBL parameters used for writing fine and coarse features in Figure 3.11 are described as follows.

- Fine feature: writing voltage = 30.0 kV, beam current = 0.154 nA, area step size = 16.0 nm, area dose $\approx 500 \mu\text{C}/\text{cm}^2$
- Coarse feature: writing voltage = 30.0 kV, beam current = 3.22 nA, area step size = 32.0 nm, area dose $\approx 700 \mu\text{C}/\text{cm}^2$

After the electron-beam exposure process had been finished, the patterns were developed in DI water/IPA at low temperature. The results are shown in Figure 3.11.

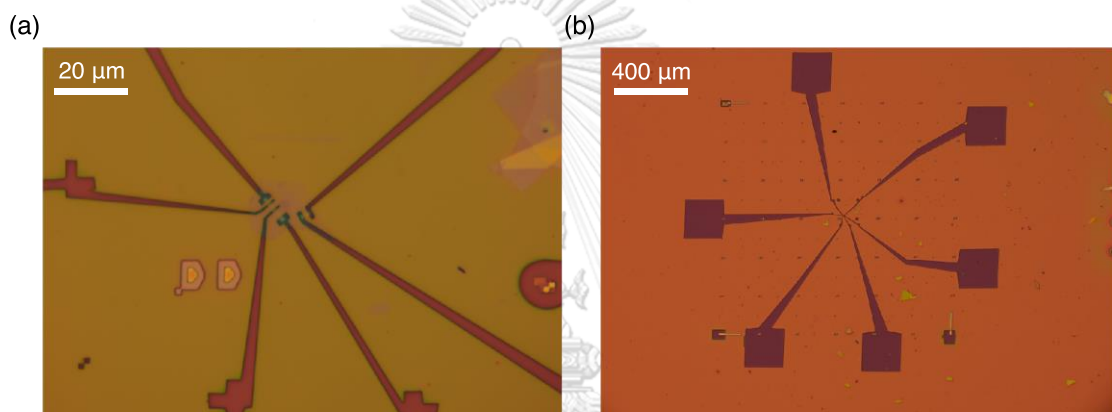


Figure 3.11 Optical images of developed patterns for (a) fine and (b) coarse features written on the BNGBN

The fine-feature pattern shown in Figure 3.11(a) consists of six electrode patterns. These six electrode patterns would be used to deposit Mo to make contacts with two BNGBNs created by plasma etching from the previous step. The smallest feature of the electrode patterns was designed to have a size of around 600 nm at the point of contact, i.e., the points at which a Mo electrode would make contact with tBLG. The electrode width was designed to have a larger size at a faraway point from the contact and connect to its coarse structure counterparts. The end of each contact has a square structure with a size of around $200 \times 200 \mu\text{m}$ as shown in Figure 3.11(b). The Mo films that would be deposited on these square structures are referred to as bonding pads, which are structures used for connecting the devices with the outside world.

3.6.1 Mo sputtering

Sputtering is a thin film deposition technique in which a surface of source material, called target, is bombarded by energetic gas particles to produce a thin film of that material on the substrate as illustrated in Figure 3.12(a).

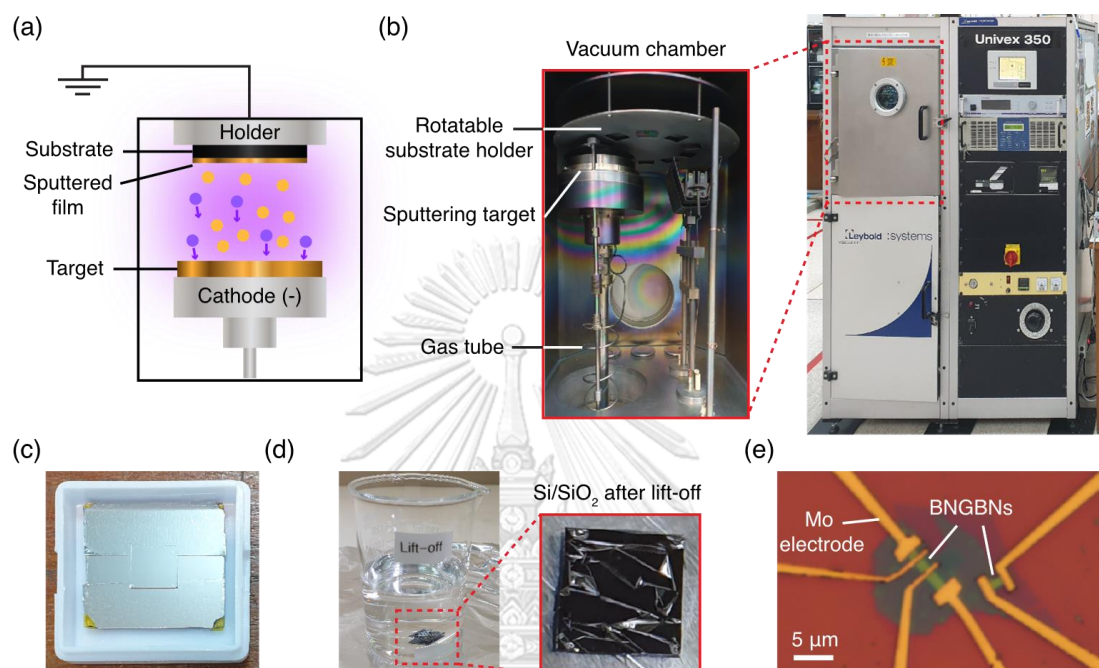


Figure 3.12(a) Basic diagram of sputtering chamber illustrating a process in which target atoms are deposited onto a substrate. Target atoms and ionized gas particles are represented by gold and purple circles, respectively. (b) Univex 350, a vacuum chamber system used for sputtering. (c) A silicon chip after the sputtering process. (d) A silicon chip in an acetone beaker. The Mo film deposited on PMMA is lifted off when PMMA has been dissolved. (e) Optical image of BNGBN with Mo electrodes obtained after lift-off process.

In this study, Mo was used as a sputtering target to deposit electrodes on the BNGBNs. Ionized Ar gas produced by a DC-plasma generator was used as sputtering gas due to its inert properties. A high-vacuum chamber system (Univex 350) integrated with a plasma generator shown in Figure 3.12(b) was employed to sputter a Mo target. The sputtering process was performed as follows. First, the silicon chip containing the BNGBNs was loaded into a vacuum chamber. Then, a turbomolecular pump along with a backing pump were used to evacuate the chamber until chamber pressure reached a designated value. The based pressure of 8.7×10^{-7} mbar was used for sputtering Mo contacts in this experiment. After the chamber pressure had reached its designated based

value, Ar gas valve was opened to let Ar gas flowed into the chamber until chamber pressure reached 6.1×10^{-3} mbar. After that, the DC-plasma generator was operated at power 550 W for 5 minutes to pre-sputter the Mo target. Pre-sputtering is a process in which the target surface is sputtered without depositing a thin film on the sample substrate, e.g., by using a shutter to shelter the substrate. This pre-sputtering session was needed to remove oxide layers that may cover the target surface. After pre-sputtering had been finished, Ar gas with a flow rate of 30 sccm (chamber pressure $\sim 7.8 \times 10^{-3}$ mbar) was introduced to dilute contaminant gas in the chamber for 10 minutes. The dilution process was followed by evacuating the chamber to its based pressure again. In the next step, the plasma generator was operated at Ar pressure 6.1×10^{-3} mbar to deposit Mo film onto the substrate. The thickness of Mo film deposited on the substrate can be determined by a deposition rate of Mo (0.91 nm/s for power 550 W). After Mo film with a thickness of 80 nm had been deposited onto the substrate, the plasma was turned off and the sample was taken out from the chamber. Figure 3.12(c) shows the silicon chip on soda-lime glass after the sputtering process where Mo film (silver-color film in the Figure) was coated on the entire surface of the chip.

3.6.1 Lift-off process

Lift-off is a method used in nanofabrication to deposit a thin film of metal onto the substrate according to a predefined pattern. In this study, the lift-off process was used to lift off the Mo film outside electrode regions from the substrate. The process can be understood by Figure 3.13(a-c). In section 3.6.1, PMMA bilayer resist had been spun onto the substrate before it was exposed to the electron beam. The effect of the difference in electron sensitivity between the two layers had been exhibited in the development process. The more electron-sensitive layer, PMMA (600K), was developed more than the less electron-sensitive layer, PMMA (950K) as schematically illustrated in Figure 13.13(a). This structure of resist is known as an undercut profile. The undercut profile prevented Mo film deposited onto Si/SiO₂ and PMMA layers to be connected as illustrated in Figure 13.13(b). The lift-off process was performed by immersing the silicon chip in acetone overnight to dissolve the PMMA film as shown in Figure 3.12(d) before spraying it with acetone to ensure that the PMMA was fully removed from the substrate. In this case, PMMA acted as sacrificial layers to remove the undesired Mo film from the substrate as depicted in Figure 13.13(c). The remaining Mo film acted as electrode contacting with the

edge of graphene as demonstrated in Figure 13.13(d). The silicon chip was then dipped in IPA for 1 minute to clean the remaining residue before blew drying with a nitrogen gun. The result after lift-off is shown in Figure 13.12(e). Figure 13.12(e) shows an optical image of two encapsulated-graphene FET devices where one of the devices has four electrodes while the other one has only two electrodes. The four-electrode device was used to investigate the transport properties of tBLG in this thesis since it has tBLG as a transport channel. The two-electrode one, however, has both MLG and tBLG parts in the transport channel and is only used to check ohmic contacts between Mo and graphene.

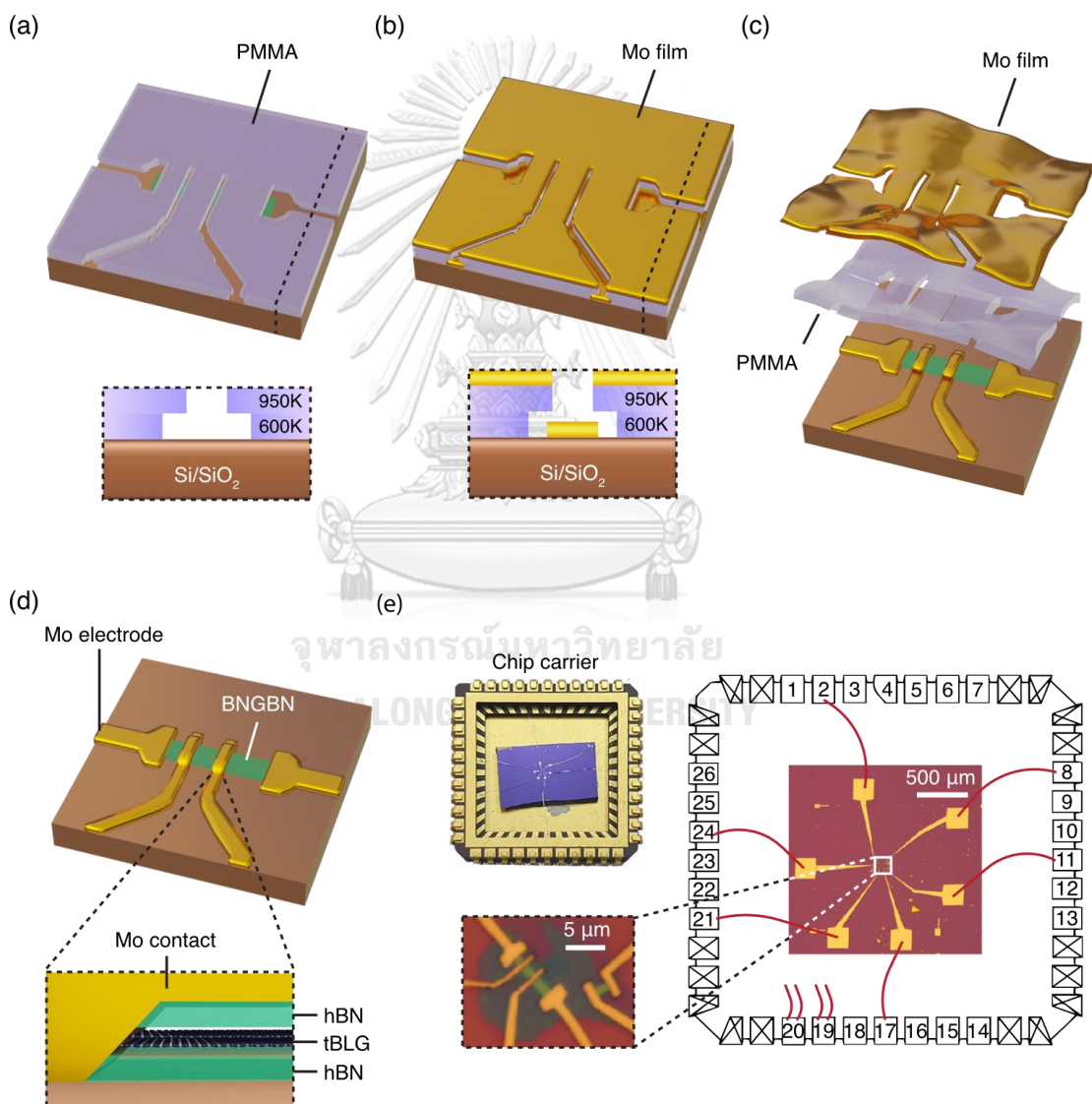


Figure 3.13 Schematics illustrating BNGBN after (a) EBL and (b) Mo sputtering. The Figures within the dash lines show the undercut profile of PMMA resist obtained by slicing the diagram in Figure 3.13(a, b) through the black dash lines. (c) A schematic of the lift-off process where Mo film outside

of the designed patterns is lifted off from the substrate with PMMA sacrificial layers. (d) A diagram illustrating edge-contact geometry between Mo and tBLG. (e) The silicon chip containing the BNGBNs on a chip carrier. The bonding pads on the chip are connected to Au pins of the chip carrier by Al wires. The right diagram demonstrates connections between Mo bonding pads and pins on the chip carrier through Al wires represented by red lines.

3.7 Wire bonding

To investigate the electronic properties of the FET devices, electrical current and voltage were applied to the devices through a chip package called chip carrier shown in Figure 3.13(e) so that the transport measurement can be performed through a chip socket using a breakout box. The silicon chip was stuck to the chip carrier using silver paint. The chip carrier consisted of 26 usable pins, made from Au, separating from each other by insulators. The numbers labeled in the diagram of Figure 3.13(e) indicate pins number on the chip carrier used to refer to electrical contact between Mo and graphene during transport measurement.

Wire bonding technique was employed to make electrical connections between Mo bonding pads on Si/SiO₂ and Au pins on a chip carrier. Al wires with a diameter of 1 mil (25.4 μm) were used to create electrical paths between the two metals. The shape of contacts between Al and metal electrodes at both ends resemble a shape of a wedge so that this technique is also known as wedge bonding. The Al wire was bonded between the two electrodes by applying ultrasonic energy and pressure onto a heated metal electrode. In this study, Al wire was firstly bonded on the chip carrier while the second bond was created on the bonding pads. The bonding parameter for the first and second bonds are described as follows.

- First bonding: ultrasonic energy = 200, bonding time = 150 ms, bonding force = 220 mN
- Second bonding: ultrasonic energy = 200, bonding time = 150 ms, bonding force = 280 mN

Both processes were performed at the substrate temperature of 98°C.

Chapter 4

Transport Measurements

The results of electrical transport measurements performed on the FET devices are shown in this chapter. The chapter begins with an experimental setup for the transport measurements. Then, Mo edge-contacts characterization will be explained. The final section discusses the results of electrical transport measurement of tBLG.

4.1 Experimental setup

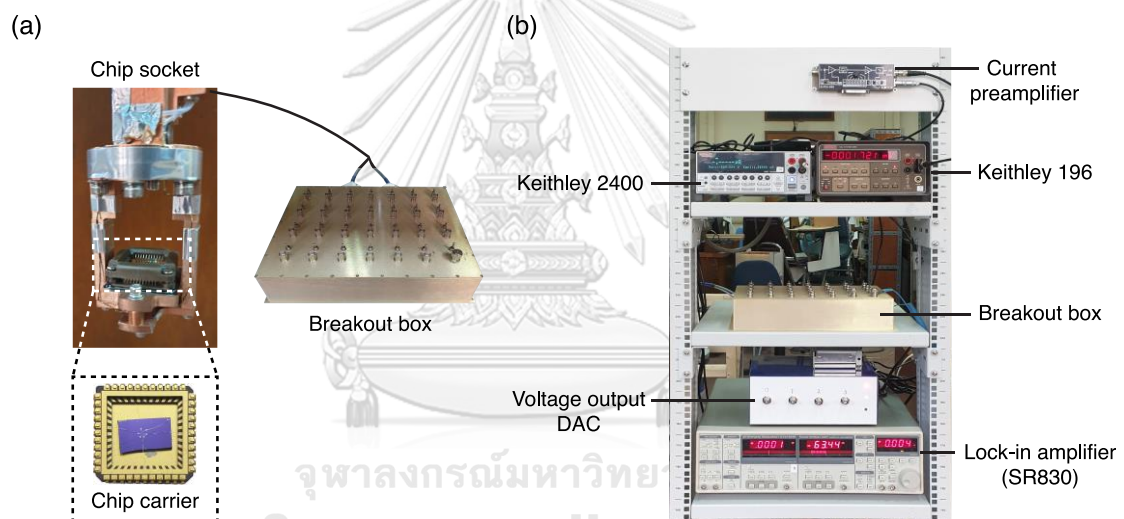


Figure 4.1 (a) A diagram showing connections between the chip carrier and a breakout box. (b) Measuring instruments used for the transport measurements.

Figure 4.1(a, b) show a basic setup for the transport measurements. The chip carrier, containing the FET devices, was put into a chip socket that electrically connected to a breakout box. On the breakout box, there are 26 switches that are directly connected to the 26 pins on the chip carrier. To apply a voltage (current) between any given pair of Mo electrodes, a voltage (current) source was connected to two switches on the breakout box that correspond to the two given electrodes using Pomona BNC connectors. Transport measurements using in this study can be classified into two types: DC measurement and AC measurement.

4.1.1 DC measurement

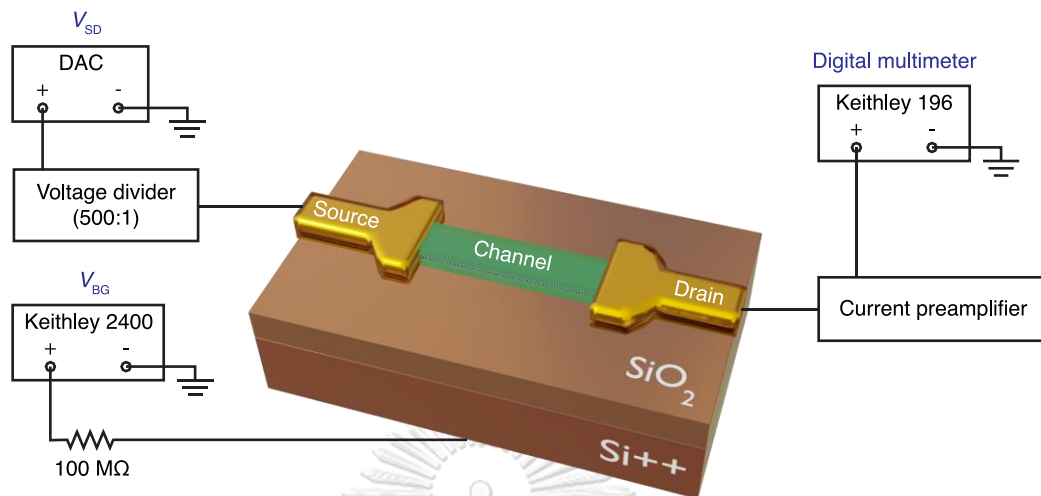


Figure 4.2 A circuit diagram demonstrating a setup for DC measurement with a bias voltage

DC measurement was employed to investigate basic characteristics of the devices such as back gate leakage current and ohmic contacts between Mo and graphene. This is to make sure that the fabricated devices were working properly before using AC measurement to probe back gate voltage-dependent properties.

A circuit diagram of the DC measurement setup is shown in Figure 4.2. A 16-bit voltage-output digital-to-analog converter (DAC) was used as a voltage source for applying a source-drain voltage, V_{SD} , to the transport channel. A voltage divider (500:1) was utilized to increase the resolution of the DAC. The current flowing through the channel was amplified with a current preamplifier to increase the signal and change it into voltage. Current to voltage gains of 10^5 and 10^7 V/A were used for contacts and leakage checking, respectively. A digital multimeter (Keithley 196) was then used to read the amplified voltage value. Keithley 2400 was employed to provide back-gate voltage, V_{BG} , to the silicon back gate. All the measuring instruments used in this study are connected to a ground of an isolation transformer to eliminate noises from the building ground.

Each instrument was controlled by a computer using IGOR Pro software. The Keithley 196 and 2400 communicated with the computer by general purpose interface buses (GPIBs) while the DAC was connected to the computer by universal serial bus (USB).

4.1.1 AC measurement

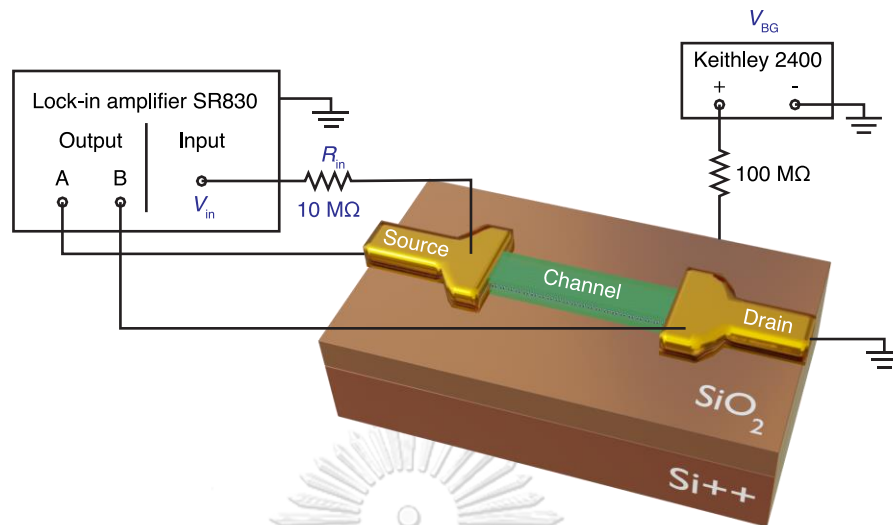


Figure 4.3 A circuit diagram demonstrating a setup for current-bias AC measurement

AC measurement is a technique widely used to attenuate noises from the environment. Figure 4.3 demonstrates a circuit diagram for the AC measurement. Here, Stanford Research System SR830 lock-in amplifier was employed to conduct the experiment. The input of SR830 provides an AC voltage with a specific frequency f_{ref} to the source of FET. To use this input as a bias current, a resistor with a resistance R_{in} was connected to the input so that the current flowing through the channel $I_{\text{in}} = V_{\text{in}} / (R_{\text{in}} + R_{\text{FET}}) \cong V_{\text{in}} / R_{\text{in}}$ did not depend on the resistance of FET, R_{FET} , if $R_{\text{in}} \gg R_{\text{FET}}$. The oscillating electric potential at source and drain electrodes were measured by outputs A and B of SR830, respectively. The output signals, which may contain noises, was then amplified in such a way that only a signal that oscillates with frequency the same as the reference frequency f_{ref} of the input was enhanced while the other signals were attenuated. The output value, $V_{\text{A-B}}$, obtained from SR830 was the root mean square (RMS) value of the source-drain voltage. In this study, a reference frequency of 17 Hz was selected to eliminate high-frequency noises, including noise from the power supply with a frequency of 50 Hz. SR830 also communicated with the computer using the GPIB port. Keithley 2400 was still employed to provide a back-gate voltage to the silicon back gate as illustrated in Figure 4.3.

4.2 Mo Contact Characterization

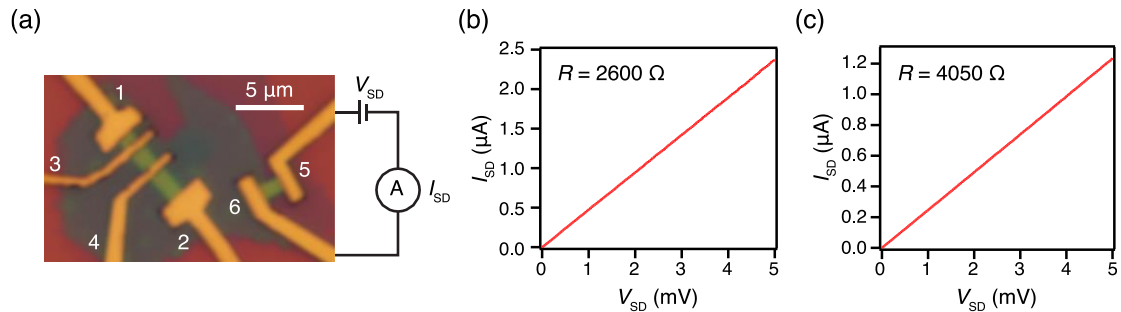


Figure 4.4(a) A circuit diagram for contact checking. The number 1-6 label contact numbers for each electrode. (b) and (c) plot relation between source-drain current and voltage measured between contact 3 – 4 and 5 – 6, respectively.

The first step for the transport measurement was to check that all the Mo electrodes properly made electrical contacts with graphene. In this step, DC measurement was used to apply bias voltage, V_{SD} , between a pair of electrodes and measure a source-drain current, I_{SD} , flowing between the two contacts. Figure 4.4(a) shows a circuit diagram for contact checking performed on electrodes number 5 and 6. The result is shown in Figure 4.4(c). The linear behavior between the current and voltage in Figure 4.4(c) follows the Ohm's law of current conduction. The contacts with this behavior are said to be ohmic. The ohmic contacts are necessary requirement for making source and drain electrodes for FET devices since ohmic contacts can conduct current in both directions. The measurement was performed on every pair of contacts for both FET devices. All the Mo electrodes fabricated in this study showed ohmic behavior. Figure 4.4(b) shows an example of ohmic contacts for contact numbers 3 and 4 of the four-electrode device.

The resistances, R , shown in Figure 4.4(b, c) were calculated from the inverse slopes of the I - V curves. These resistances were a combination of the channel resistances and contact resistances which depended on the voltage of the silicon back gate. However, applying back-gate voltage may create an unwanted electrical path from the back gate to the transport channel as shown as a white dash line in Figure 4.5(a). This parasitic current is known as leakage current. To check the amount of the leakage current, V_{BG} , was applied to the silicon back gate, sweeping from 60 to -60 V (1200 points with a sweep rate of 10 points/s). The current flow through contact 4 was measured for each value of V_{BG} . The result is shown in Figure 4.5(b). The amount of leakage current

varied in the order of 10 pA far below the typical current use in the transport measurement which is in the order of μA . This means that the electron density in graphene can be tuned by V_{BG} in the range of -60 to +60 V without dielectric breakdown.

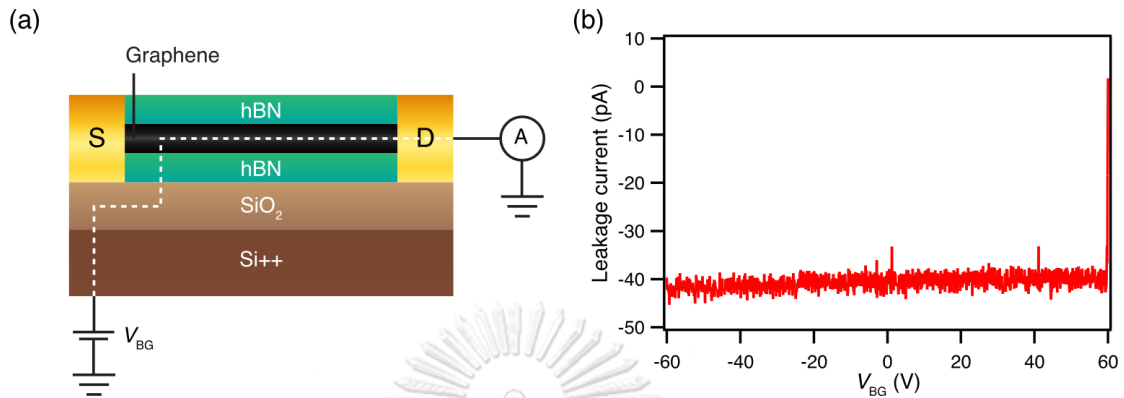


Figure 4.5(a) A diagram shows an electrical path of the back-gate leakage current (white dash line). (b) Back-gate leakage current flow through contact 4 as a function of V_{BG} .

The four-electrode device was used to characterize contact quality and investigate transport properties of tBLG. Figure 4.6(a) demonstrates an experimental setup for extracting contact resistance between contact 3 and the tBLG channel. First, AC measurement with a bias current, I_{34} , of 100 nA was applied between contact 3 and 4. The voltage V_{34} across the two contacts was measured as a function of V_{BG} . The measure resistance $R_{34} = V_{34}/I_{34}$ across can be expressed as

$$R_{34} = R_{C3} + R_{\text{tBLG}} + R_{C4}, \quad (4.1)$$

where R_{tBLG} is a resistance of tBLG and R_{C_i} is a contact resistance between contact i and tBLG. In addition to V_{34} , a voltage V_{14} between contact 1 and 4 was also measured to derive the resistance $R_{14} = V_{14}/I_{34}$,

$$R_{14} = R_{\text{tBLG}} + R_{C4}. \quad (4.2)$$

The contact resistance R_{C3} between contact 3 and tBLG can be obtained by subtracting the above two equations, $R_{C3} = R_{34} - R_{14}$. Since contact resistance is a quantity that depends on a contact width [35], R_{C3} was multiply with the contact width (1.5 μm for contact 3) to derive the geometry-independent contact resistivity ρ_C . The result of the experiment is shown in Figure 4.6(b).

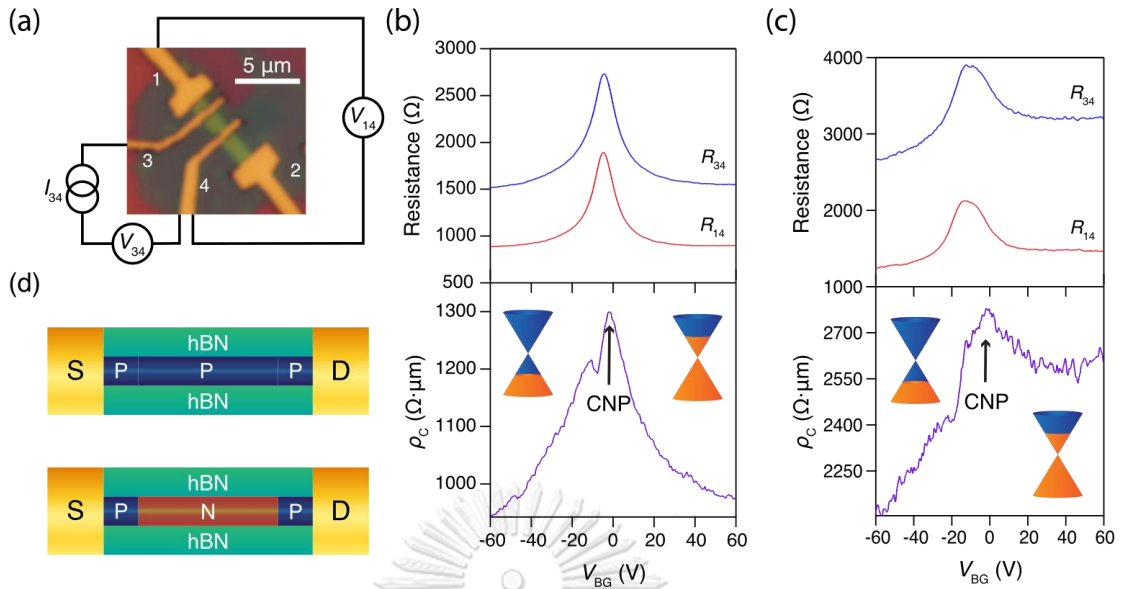


Figure 4.6(a) A diagram for measurement setup for probing contact resistance between contact 3 and tBLG. (b, c) show measured resistance R_{34} , R_{14} and calculated contact resistivity ρ_c as functions of V_{BG} obtained immediately after fabrication (b) and after 57 days after the first measurement. The insets in Figure 4.6(b, c) are Dirac cones illustrated filled states (orange) in the band structure at negative and positive values of V_{BG} . (d) Schematics illustrate the behavior of the transport channel when V_{BG} is tuned to negative (top) and positive (bottom) values. The P and N regions are regions in tBLG where the majority charge carriers are holes and electrons, respectively.

The relation between V_{BG} and carrier density, n , in tBLG can be estimated by Equation (2.11) using $d_1 = 285$ nm, $d_2 = 20$ nm, $\epsilon_{r1} = 3.7$ and $\epsilon_{r2} = 3.2$ [36]. The observed contact resistivity in Figure 4.6(b) was found to depend on the carrier density. The contact resistivity reached the maximum value of around $1,300 \text{ } \Omega \cdot \mu\text{m}$ at charge neutrality point (CNP), a point in which the valence band is filled and the conduction band is empty, and decreased to $975 \text{ } \Omega \cdot \mu\text{m}$ at 60 V away from CNP which corresponds to carrier density of around $4 \times 10^{12} \text{ cm}^{-2}$. This result is comparable to encapsulated devices that were fabricated by using Cr/Au as edge-contact whose contact resistivity varied between 200 - $2,000 \text{ } \Omega \cdot \mu\text{m}$ [11] at the same range of carrier density.

The experiment was conducted again after 57 days from the first experiment. Figure 4.6(c) shows the result of the later experiment where the two-fold increase in contact resistivity was observed. This time, however, there was asymmetry in contact resistivity around CNP when charge carriers changed between electrons and holes. The contact resistivity for electrons was larger than holes at the same carrier density. This

asymmetry in contact resistivity has been reported for high-work function metals such as Au and Pd [11, 37]. The mechanism for this behavior can be understood by the charge transfer process described in chapter 2. When a high-work function metal is brought into contact with graphene, electrons in graphene are transferred across the contact interface to the metal. This process is a result of the higher energy of electrons in graphene compared to that of metal. The charge transfer process continues until the Fermi energy of electrons in the graphene-metal system reaches its equilibrium. This will create a hole-doped region at the vicinity of the contact as shown in Figure 4.6(d). When charge carriers in tBLG are holes, the current can easily flow across the contact. However, when the charge carriers are gated electrons, the electrons traveling across the contact feel the potential barrier created by the hole-doped region at the contact. In this case, the contact interface acts as a PN junction increasing the total resistance of the device.

When the experiment was first performed after the fabrication process, the contact resistivity curve had symmetry around CNP. This situation is expected because the work function of Mo is approximately the same as tBLG [13, 28]. Therefore, there should be a very small charge transfer at the contact interface. As for the contact resistivity curve in Figure 4.6(c), we argue that the asymmetry is a result of the oxidization of the Mo contact into MoO_x . The large difference between the work function of tBLG (~ 4.5 eV) and MoO_x (~ 6.8 eV for MoO_3) causes a large charge transfer at the contact interface resulting in the asymmetry in the contact resistivity. Nevertheless, all the contacts between Mo and tBLG still exhibited ohmic behavior after they had been fabricated for 3 months.

4.3 Charge transportation in tBLG

Despite the degradation of Mo contacts, transport characteristics of tBLG can still be obtained by using a four-probe measurement. Figure 4.7(a) shows a setup for four-probe measurement. The current bias, I_{12} , of 100 nA was applied between contact 1 and 2 and the voltage, V_{34} , between contact 3 and 4 was measured as a function of the back-gate voltage V_{BG} . V_{BG} was sweeping between -40 to +40 V (800 points with sweep rate 10 points/s). Since there was no current flowing across contact 3 and 4 due to the large resistance of the voltmeter, the measured resistance, $R_{34} = V_{34}/I_{12}$, was the pure resistance of tBLG.

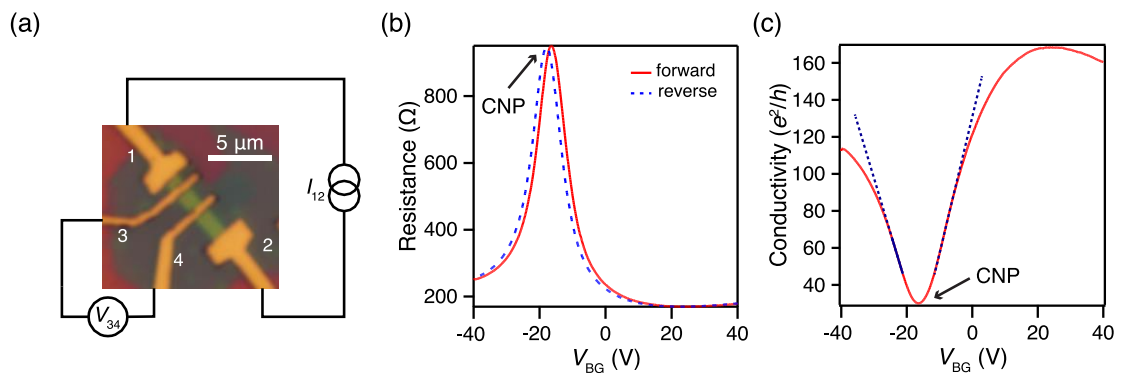


Figure 4.7(a) A four-probe measurement setup for investigating transport characteristics of tBLG. (b) Resistance of tBLG measure between contact 3 and 4 as a function of V_{BG} . (c) Conductivity of tBLG. The blue dash lines show the slope of conductivity used for calculating electron and hole mobility.

The result of the four-probe measurement performed after the device had been fabricated for 3 months is shown in Figure 4.7(b). The first thing to consider is the position of CNP. When the device was measured for the first time immediately after the fabrication process, the CNP had located near $V_{BG} = 0$. On the contrary, the CNP shown in Figure 4.7(b), indicated by the resistance peak, was shifted to $V_{BG} \sim 16$ V. This implies that at zero back-gate voltage the Fermi energy of electrons in graphene did not locate at the Dirac points. This also indicates that the device was somehow doped with electrons over time. The electron doping contradicts the hole doping from the charge transfer at the contact interface. We discuss that the electron doping may be caused by the exposed σ bond at the edges of graphene reacting with ambient contamination in the air resulting in H-terminated edges. The H-terminated edges then donated electrons to tBLG leading to the shift in CNP [38]. Even after such doping, the device exhibited very small hysteresis when V_{BG} was forward and reverse sweeping. This small hysteresis is a consequence of encapsulated structure that prevents external impurities at the device surface to affect the transport characteristics of tBLG.

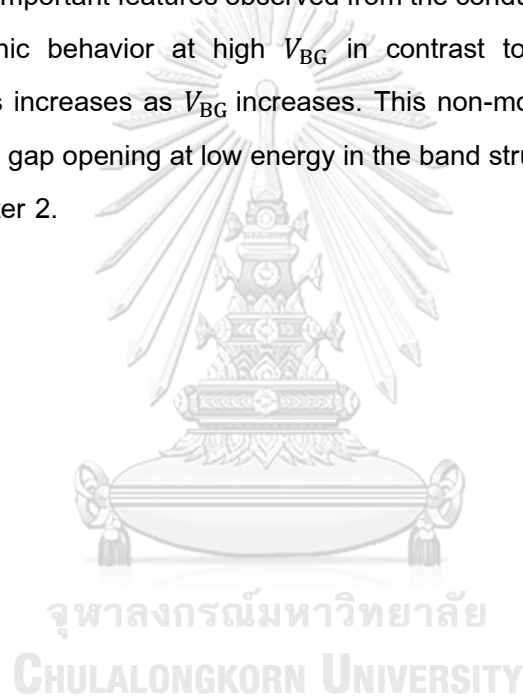
Conductivity, σ , was calculated from the resistance graph to extract the intrinsic transport properties of tBLG as shown in Figure 4.7(c). The back-gate voltage dependent conductivity can be used to calculate field-effect mobility

$$\mu = \frac{1}{C} \frac{\partial \sigma}{\partial V_{BG}} \quad (4.2)$$

where the capacitance per unit area C was calculated from Equation (2.11). The formula in Equation (4.2) was derived from the Drude model of electrical conduction. The field-

effect mobility was used instead of Hall mobility in this thesis since it can extract the carrier mobility without relying on magnetic field as demonstrated in Ref. [10, 39]. In this thesis carrier mobility was extracted from the slope of the linear region of the conductivity curve shown as blue dash lines in Figure 4.7(c). We obtained the room-temperature electron and hole mobility of around 27,000 and 21,000 $\text{cm}^2/\text{V}\cdot\text{s}$. This result is comparable to the reported value obtained from encapsulated MLG devices which have a room-temperature electron mobility of $\sim 40,000 \text{ cm}^2/\text{V}\cdot\text{s}$ [11] indicating that Mo electrodes do not hinder the quality of tBLG.

One of the important features observed from the conductivity curve in Figure 4.7(c) is its non-monotonic behavior at high V_{BG} in contrast to BLG devices, where the conductivity always increases as V_{BG} increases. This non-monotonic behavior may be a result of the energy gap opening at low energy in the band structure of tBLG as previously mentioned in chapter 2.



Chapter 5

Conclusions

This chapter concludes the experiments we have done so far in this thesis. It summarizes the topic of device fabrication, characterization of Mo electrodes and room-temperature electrical transport properties of tBLG.

The first topic is device fabrication. We have fabricated two FET devices using edge-contact geometry. Mo was selected as an alternative electrode for graphene due to its good electrical properties. One of the devices has tBLG as a charge transport channel. The materials that were used to create the FETs, graphene and hBN, were obtained by mechanical exfoliation. tBLG was created from a single flake of MLG using the tear-and-stack technique. Two hBN flakes were used to form and encapsulate the tBLG protecting it from external impurities. The formation of the twisted structure of graphene has been confirmed by Raman spectroscopy. To make electrical connections between tBLG and Mo electrodes, EBL was employed to define device structure. The edge of the encapsulated tBLG was then exposed by O_2/CHF_3 plasma to make 1D contact with Mo electrodes by DC sputtering.

Room-temperature electrical transport measurements were used to characterize the quality of Mo edge-contacts. All the Mo contacts fabricated in this study exhibited ohmic behavior. We have found that contact resistivity between Mo and graphene depends on carrier density in the transport channel. The contact resistivity varied in the range of around $1,000 - 1,300 \Omega \cdot \mu m$ for a carrier density in the range of $\pm 4 \times 10^{12} \text{ cm}^{-2}$. The values of contact resistivity observed in this study are comparable to that of previous reports. However, we have observed that the contact resistivity increases over time likely due to the oxidization of Mo.

Despite the increase in contact resistivity, the edge-contacts still remains ohmic and four-probe measurement can still be used to investigate transport properties of tBLG. The room-temperature mobilities of tBLG reached the value as high as 27,000 and 21,000 $\text{cm}^2/\text{V}\cdot\text{s}$ for electron and hole, respectively. This high mobility indicates that Mo contacts

have negligible effects on charge transportation in graphene. We have found that Mo electrodes can be utilized to observe the unusual effect such as the non-monotonic behavior of conductivity at high electron density. These results demonstrate that Mo can be used as an alternative electrode for graphene expanding a possibility for device fabrication.



REFERENCES

1. Frank, D.J., Y. Taur, and H.-S. Wong, *Generalized scale length for two-dimensional effects in MOSFETs*. IEEE Electron Device Letters, 1998. **19**(10): p. 385-387.
2. Novoselov, K., et al., *2D materials and van der Waals heterostructures*. Science, 2016. **353**(6298).
3. Novoselov, K.S., et al., *Electric field effect in atomically thin carbon films*. science, 2004. **306**(5696): p. 666-669.
4. Novoselov, K.S., et al., *Two-dimensional gas of massless Dirac fermions in graphene*. nature, 2005. **438**(7065): p. 197-200.
5. Young, A.F. and P. Kim, *Quantum interference and Klein tunnelling in graphene heterojunctions*. Nature Physics, 2009. **5**(3): p. 222-226.
6. Zhang, Y., et al., *Direct observation of a widely tunable bandgap in bilayer graphene*. Nature, 2009. **459**(7248): p. 820-823.
7. Akinwande, D., et al., *Graphene and two-dimensional materials for silicon technology*. Nature, 2019. **573**(7775): p. 507-518.
8. Cao, Y., et al., *Unconventional superconductivity in magic-angle graphene superlattices*. Nature, 2018. **556**(7699): p. 43-50.
9. Zhang, Y., et al., *Origin of spatial charge inhomogeneity in graphene*. Nature Physics, 2009. **5**(10): p. 722-726.
10. Dean, C.R., et al., *Boron nitride substrates for high-quality graphene electronics*. Nature nanotechnology, 2010. **5**(10): p. 722-726.
11. Wang, L., et al., *One-dimensional electrical contact to a two-dimensional material*. Science, 2013. **342**(6158): p. 614-617.
12. Zhang, Y. and X.-P. Qu, *Improved contact resistivity and enhanced mobility of metal-graphene FET by inserting ultra-thin MoO_x layer at source/drain region*. AIP Advances, 2019. **9**(5): p. 055221.

13. Yoo, G., et al., *Electrical contact analysis of multilayer MoS₂ transistor with molybdenum source/drain electrodes*. IEEE Electron Device Letters, 2015. **36**(11): p. 1215-1218.
14. Lee, C., et al., *Measurement of the elastic properties and intrinsic strength of monolayer graphene*. science, 2008. **321**(5887): p. 385-388.
15. Zhang, Y., et al., *Experimental observation of the quantum Hall effect and Berry's phase in graphene*. nature, 2005. **438**(7065): p. 201-204.
16. Wallace, P.R., *The band theory of graphite*. Physical review, 1947. **71**(9): p. 622.
17. Yao, W., et al., *Quasicrystalline 30° twisted bilayer graphene as an incommensurate superlattice with strong interlayer coupling*. Proceedings of the National Academy of Sciences, 2018. **115**(27): p. 6928-6933.
18. Cao, Y., et al., *Correlated insulator behaviour at half-filling in magic-angle graphene superlattices*. Nature, 2018. **556**(7699): p. 80-84.
19. Bistritzer, R. and A.H. MacDonald, *Moiré bands in twisted double-layer graphene*. Proceedings of the National Academy of Sciences, 2011. **108**(30): p. 12233-12237.
20. Tarnopolsky, G., A.J. Kruchkov, and A. Vishwanath, *Origin of magic angles in twisted bilayer graphene*. Physical review letters, 2019. **122**(10): p. 106405.
21. Cao, Y., et al., *Superlattice-induced insulating states and valley-protected orbits in twisted bilayer graphene*. Physical review letters, 2016. **117**(11): p. 116804.
22. Kim, K., et al., *van der Waals heterostructures with high accuracy rotational alignment*. Nano letters, 2016. **16**(3): p. 1989-1995.
23. Nam, N.N. and M. Koshino, *Lattice relaxation and energy band modulation in twisted bilayer graphene*. Physical Review B, 2017. **96**(7): p. 075311.
24. Nery, J.P., M. Calandra, and F. Mauri, *Long-range rhombohedral-stacked graphene through shear*. Nano Letters, 2020. **20**(7): p. 5017-5023.
25. Ferrari, A.C. and D.M. Basko, *Raman spectroscopy as a versatile tool for studying the properties of graphene*. Nature nanotechnology, 2013. **8**(4): p. 235-246.

26. Kim, K., et al., *Raman spectroscopy study of rotated double-layer graphene: misorientation-angle dependence of electronic structure*. Physical review letters, 2012. **108**(24): p. 246103.
27. Moutinho, M.V., P. Venezuela, and M.A. Pimenta, *Raman Spectroscopy of Twisted Bilayer Graphene*. C, 2021. **7**(1): p. 10.
28. Robinson, J.T., et al., *Work function variations in twisted graphene layers*. Scientific reports, 2018. **8**(1): p. 1-9.
29. Taniguchi, T. and K. Watanabe, *Synthesis of high-purity boron nitride single crystals under high pressure by using Ba–BN solvent*. Journal of crystal growth, 2007. **303**(2): p. 525-529.
30. Huang, Y., et al., *Reliable exfoliation of large-area high-quality flakes of graphene and other two-dimensional materials*. ACS nano, 2015. **9**(11): p. 10612-10620.
31. Nair, R.R., et al., *Fine structure constant defines visual transparency of graphene*. Science, 2008. **320**(5881): p. 1308-1308.
32. Wang, Y.Y., et al., *Thickness identification of two-dimensional materials by optical imaging*. Nanotechnology, 2012. **23**(49): p. 495713.
33. Purdie, D., et al., *Cleaning interfaces in layered materials heterostructures*. Nature communications, 2018. **9**(1): p. 1-12.
34. Cuscó, R., et al., *Temperature dependence of Raman-active phonons and anharmonic interactions in layered hexagonal BN*. Physical Review B, 2016. **94**(15): p. 155435.
35. Nagashio, K., et al. *Metal/graphene contact as a performance killer of ultra-high mobility graphene analysis of intrinsic mobility and contact resistance*. in *2009 IEEE International Electron Devices Meeting (IEDM)*. 2009. Ieee.
36. Campos, L., et al., *Quantum and classical confinement of resonant states in a trilayer graphene Fabry-Pérot interferometer*. Nature communications, 2012. **3**(1): p. 1-6.
37. Xia, F., et al., *The origins and limits of metal–graphene junction resistance*. Nature nanotechnology, 2011. **6**(3): p. 179-184.

38. Brenner, K., Y. Yang, and R. Murali, *Edge doping of graphene sheets*. Carbon, 2012. 50(2): p. 637-645.
39. Taychatanapat, T., et al., *Quantum Hall effect and Landau-level crossing of Dirac fermions in trilayer graphene*. Nature Physics, 2011. 7(8): p. 621-625.





จุฬาลงกรณ์มหาวิทยาลัย
CHULALONGKORN UNIVERSITY

VITA

NAME	Illias Klanurak
DATE OF BIRTH	19 November 1995
PLACE OF BIRTH	Songkhla, Thailand
INSTITUTIONS ATTENDED	Chulalongkorn University
HOME ADDRESS	Department of Physics, Faculty of Science, Chulalongkorn University, Phayathai Rd., Patumwan, Bangkok 10330, Thailand

